Research Square

Preprints are preliminary reports that have not undergone peer review.
They should not be considered conclusive, used to inform clinical practice,
or referenced by the media as validated information.

Deep proteomics profiling of the cell secretome by DeepSec

Amir Ata Saei

amir.saei@ki.se

Karolinsk a Institute https://orcid.org/0000-0002-2639-6328

Xueyao Wang

Karolinska Institutet

Konstantinos Fragkoulis

Karolinska Institutet https://orcid.org/0009-0003-3564-8560

Aleksandra Wielento

Karolinska Institutet

Sabine Willems

Karolinska Institutet

Marie-Stéphanie Aschtgen

Karolinska Institutet

Anna Kirk

Karolinska Institutet

Seyed Majed Modaresi

Broad Institute https://orcid.org/0000-0001-9747-9748

Hassan Gharibi

Karolinska Institute

Mohieddin JAFARI

University of Helsinki https://orcid.org/0000-0002-6991-8587

Danilo Ritz

Biozentrum, University of Basel, Basel, Switzerland; https://orcid.org/0009-0004-8603-9754

Alexander Schmidt

Biozentrum, University of Basel https://orcid.org/0000-0002-3149-2381

Hojatollah Vali

Department of Anatomy and Cell Biology, McGill University

Jutta Jalkanen

Karolinska Institutet

Mikael Rydén

Karolinska Institutet

Niklas Mejhert

Karolinska Institutet

Volker Lauschke

Karolinska Institutet https://orcid.org/0000-0002-1140-6204

Babak Borhan

Michigan State University https://orcid.org/0000-0002-3193-0732

Morteza Mahmoudi

Precision Health Program, Michigan State University

Sylvain Peuget

Karolinksa Institutet https://orcid.org/0000-0002-3315-1935

Article

Keywords: nanoparticle, protein corona, mass spectrometry, secreted, monocytes, cytokines

Posted Date: July 21st, 2026

DOI: https://doi.org/10.21203/rs.3.rs-10362172/v1

License: This work is licensed under a Creative Commons Attribution 4.0 International License.
Read Full License

Additional Declarations: Yes there is potential Competing Interest. M.M. discloses that (1) he is a co-founder and director of the Academic Parity Movement (www.paritymovement.org), a non-profit organization dedicated to addressing academic discrimination, violence and incivility; (2) he is a co-founder of and shareholder in Targets' Tip, AlbuDerm, and XProteome Inc.; and (3) he receives royalties/honoraria for his published books, plenary lectures and licensed patents. A.A.S. and B.B. are co-founders of XProteome, Inc. V.M.L. is co-founder, CEO and shareholder of HepaPredict AB, as well as co-founder and shareholder of Shanghai Hepo Biotechnology Ltd.

Deep proteomics profiling of the cell secretome by DeepSec

Xueyao Wang[1], Konstantinos Fragkoulis[1], Aleksandra Wielento[1], Sabine Willems[2], Marie-Stéphanie Aschtgen[1], Anna Kirk[1], Seyed Majed Modaresi[3,4,5], Hassan Gharibi[6], Mohieddin Jafari[7,8,9], Danilo Ritz[10], Alexander Schmidt[10], Hojatollah Vali[11,12], Jutta Jalkanen[13], Mikael Rydén[13], Niklas Mejhert[13], Volker M. Lauschke[2,14,15,16], Babak Borhan[17], Morteza Mahmoudi[18,19*], Sylvain Peuget[1*], Amir Ata Saei[1*]

[1]Department of Microbiology, Tumor and Cell Biology, Karolinska Institutet, 171 65 Stockholm, Sweden
[2]Department of Physiology and Pharmacology and Center for Molecular Medicine, Karolinska Institutet and University Hospital, Stockholm, Sweden
[3]Infectious Disease and Microbiome Program, Broad Institute of MIT and Harvard, Cambridge, MA 02142, USA
[4]Institute for Medical Engineering & Science and Department of Biological Engineering, Massachusetts Institute of Technology, Cambridge, MA 02139, USA
[5]Wyss Institute for Biologically Inspired Engineering, Harvard University, Boston, MA 02115, USA
[6]Division of Chemistry I, Department of Medical Biochemistry and Biophysics, Karolinska Institutet, 171 65 Stockholm, Sweden
[7]Department of Pharmacology, Faculty of Medicine, University of Helsinki, Helsinki, Finland
[8]Faculty of Medicine and Health Technology, Tampere University, Tampere, Finland
[9]Tampere Institute for Advanced Study, Tampere University, Tampere, Finland
[10]Proteomics Core Facility, Biozentrum, University of Basel, Basel, Switzerland
[11]Department of Anatomy and Cell Biology, McGill University, Montreal, QC, H3A 0C7, Canada
[12]Facility for Electron Microscopy Research, McGill University, Montreal, QC, H3A 0C7, Canada
[13]Department of Medicine (H7), Karolinska Institutet, C2-94 and Medical Unit Endocrinology, Karolinska University Hospital Huddinge, 141 86 Stockholm, Sweden
[14]Dr. Margarete Fischer-Bosch Institute of Clinical Pharmacology, Stuttgart, Germany
[15]University of Tübingen, Tübingen, Germany
[16]Department of Pharmacy, the Second Xiangya Hospital, Central South University, Changsha, China
[17]Department of Chemistry, Michigan State University, East Lansing, Michigan 48824, USA
[18]Precision Health Program, Michigan State University, East Lansing, MI, USA
[19]Department of Radiology, College of Human Medicine, Michigan State University, East Lansing, MI, USA

Equal contribution: XW and KF
Correspondence to: Mahmou22@msu.edu, Sylvain.Peuget@ki.se and Amir.Saei@ki.se

Abstract

Cellular secretome profiling is essential for decoding intercellular communication, identifying disease biomarkers, and discovering therapeutic targets. Although mass spectrometry-based proteomics is the gold standard for discovery-driven analysis, deep secretome profiling remains technically challenging because low-abundance signaling molecules are masked by the vast dynamic range of high-background serum supplements. To overcome these limitations, we develop DeepSec, a robust and streamlined method that uses a small-molecule–modulated nanoparticle protein corona to selectively deplete bovine serum albumin from conditioned media. Using an endogenous lipopolysaccharide (LPS) dose-response series, DeepSec preserved biological fold changes relative to a non-depleted workflow and orthogonal ELISA, establishing protein-corona enrichment as a quantitatively faithful strategy for dynamic secretome proteomics. In parallel, DeepSec increased the number of significantly secreted proteins by three-fold. We demonstrate its utility for profiling secretomes from cultured cells and host–pathogen interaction models. Using pathway-specific inhibitors, we further resolve proteins secreted through ER–Golgi- and autophagy-dependent routes following LPS stimulation. Finally, we show the translational utility of DeepSec by profiling patient-derived 3D liver microtissues modeling metabolic dysfunction-associated steatohepatitis, capturing distinct, drug-specific metabolic and extracellular matrix rewiring patterns in response to clinical therapeutics. These results establish DeepSec as a robust platform for interrogating complex extracellular signaling networks across diverse models of health and disease.

Keywords: nanoparticle, protein corona, mass spectrometry, secreted, monocytes, cytokines

1. Introduction

The secretome encompasses the full repertoire of molecules that cells secrete into their surroundings, including both actively secreted molecules and those passively released during cellular turnover or stress, which can serve as “molecular messages” to biosystems (e.g., cells and tissues) (*1*). Among these molecules, secreted proteins such as cytokines, chemokines, growth factors, and hormones orchestrate key biological processes including immune regulation, tissue repair, and development (*2*). Secretome profiling enables the identification of disease-associated biomarkers and therapeutic targets; for instance, TNF-α and IL-6 can serve as indicators of pathological activity and represent actionable targets for drug development for the treatment of autoimmune diseases (*3*). In cancer, secretome analysis reveals how tumors remodel their microenvironment, promoting angiogenesis, suppressing immune surveillance, and altering the extracellular matrix (*4*, *5*). Similarly, in host–pathogen interactions, profiling secreted proteins can illuminate how the host cells respond to infections or how infections modulate immune responses (*6*, *7*).

However**,** comprehensive secretome profiling remains technically challenging. Although mass spectrometry (MS)–based proteomics is the gold standard for proteome analysis (*8*), in cell culture, serum supplements such as fetal bovine serum (FBS) introduce abundant background proteins (e.g., bovine albumin) that can mask low-abundance secreted proteins. The broad dynamic range between low-abundance secreted proteins and high-abundance serum-derived proteins limits MS sensitivity. While serum-free media avoid this background, they are non-physiological and can

stress cells, causing death and release of intracellular contaminants (*8*). Common enrichment methods (e.g., filter-aided concentration or protein precipitation) can improve sensitivity, but risk protein loss or introduce bias (*9*). These limitations highlight the need for development of reproducible methods that enable deep, discovery-driven secretome profiling under physiologically relevant, serum-containing conditions. While recent antibody-based or other multiplexed platforms enable sensitive quantification of predefined panels of cytokines and other secreted proteins (*10*), MS-based approaches remain preferable for discovery-driven secretome analysis.

The nanoparticle protein corona, the layer of proteins that forms on the surface of nanoparticles in biological fluids, offers a promising solution for selective protein enrichment (*11*). Previous studies have shown that nanoparticles can selectively enrich low-abundance proteins, enhancing the depth of proteomics profiles (*12*–*15*). We recently demonstrated that small molecule adjuvants such as phosphatidylcholine, can block the interaction sites of albumin to the surface of nanoparticles and therefore boost their capability in enrichment of low-abundance proteins, increasing the number of quantified plasma proteins by ~50% across various MS platforms (*14*, *16*).

Here we introduce DeepSec, a first-of-its-kind nanoparticle-enabled workflow for deep and discovery-driven secretome profiling under physiologically relevant conditions. DeepSec exploits tailored small-molecule–modulated nanoparticle–protein interactions without the need for serum-free culture or harsh depletion strategies. This is combined with sequential low- and high-speed centrifugation to efficiently remove cell- and debris-derived contaminants prior to enrichment. This approach expands detectable secretome coverage more than threefold while using the same downstream LC–MS acquisition and data-analysis workflow, providing unprecedented access to the signaling complexity of secreted proteins.

We comprehensively benchmark DeepSec against standard workflows across multiple performance metrics, including sensitivity, coefficient of variation and quantitative accuracy. Using THP1 macrophages stimulated with a titration series of *Klebsiella pneumoniae* lipopolysaccharide (LPS), we demonstrate that small-molecule–modulated nanoparticle-based sample preparation preserves quantitative differences across biological states, with fold changes measured by DeepSec closely matching orthogonal ELISA measurements. As part of this benchmarking, DeepSec accurately detects the secretion of serum amyloid A1 (SAA1) from adipocytes upon LPS stimulation (*17*). We further demonstrate the versatility of DeepSec by characterizing proteins secreted through ER–Golgi and autophagy-dependent pathways following LPS stimulation and by simultaneously profiling host and bacterial proteomes across host–pathogen interaction models. Finally, we demonstrate the utility of DeepSec to monitor therapeutic responses by profiling the secretome of *ex vivo* human liver microtissues of patients with metabolic dysfunction–associated steatohepatitis (MASH) in response to FDA-approved and experimental therapeutics. By enabling high depth, sensitivity, reproducibility and quantitative accuracy, DeepSec provides a powerful platform for investigating intercellular and inter-organ communication in health and disease.

Results

2.1. DeepSec sensitivity, reproducibility and quantitative accuracy

The DeepSec workflow is outlined in **Fig 1a**. To establish and benchmark the technique, THP1-derived macrophages were cultured in complete medium containing

10% FBS and stimulated with serial concentrations of LPS from *K. pneumoniae* for 8 h with no discernible cell death. Cell supernatants were sequentially centrifuged at 300 g for 5 min to remove floating cells, then at 10,000 g to remove cell debris. Adherent cells were also collected for cell proteome analysis. For the cell proteome, we quantified 7505 proteins with at least 2 peptides using TMT multiplexing (**Supplementary Data 1**). The conditioned medium was then used for parallel secretome analysis by routine digestion (standard approach), or small molecule-nanoparticle-based depletion of highly abundant proteins, followed by digestion (DeepSec). Cryo-TEM supported the formation of corona-coated nanoparticles without detectable vesicular structures or large protein aggregates under the conditions examined (**Supplementary Fig 1**). Full characterization of these nanoparticles has been conducted in our prior publications (*16*, *18*, *19*).

DeepSec showed a significantly higher sensitivity compared to the standard approach and could detect an average of 1992 proteins vs. 659 proteins before applying the stricter peptide-count filter (**Fig 1b-c; Supplementary Data 2-3**). Interestingly, the sheer number of proteins in the treated LPS-stimulated samples was higher, indicating the secretion of proteins absent from the secretome of untreated cells, validating our methodology. The marked increase in secretome coverage stems from effective depletion of highly abundant proteins such as bovine albumin, lactotransferrin, hemoglobin, alpha-2-macroglobulin, alpha-fetoprotein and serotransferrin (**Fig 1d**), which dominate standard workflows based on normalized intensity. To ensure an unbiased comparison, the latter analysis was based on a unified database search of standard and DeepSec MS .raw files (**Supplementary Data 4**).

The median coefficient of variation (CV) of the intensity of all detected proteins was 4.25% for the cell proteome, 11.83% for the standard secretome and 19.78% for the DeepSec samples (**Fig 1e**). A higher CV for DeepSec is expected due to the inclusion of lower abundance proteins, as we approach the limit of detection. Generally, there was a high Pearson correlation between replicates in DeepSec (**Fig 1e**, right panel). As expected, principal component analysis (PCA) of the cell proteome and secretome data showed that the main driver of separation is the LPS concentration (**Fig 1f**), and that DeepSec maintains a high level of quantitative accuracy. The number of significant secreted proteins (arbitrary cutoff of log2 fold change >0.5 and FDR <0.05) also increased 3-fold at the highest LPS concentration (**Fig 1g**, **Supplementary Data 2-3**). Moreover, fold changes for proteins quantified by standard and DeepSec workflows strongly correlated ($r = 0.80$), further indicating that DeepSec preserves quantitative accuracy (**Fig 1h**).

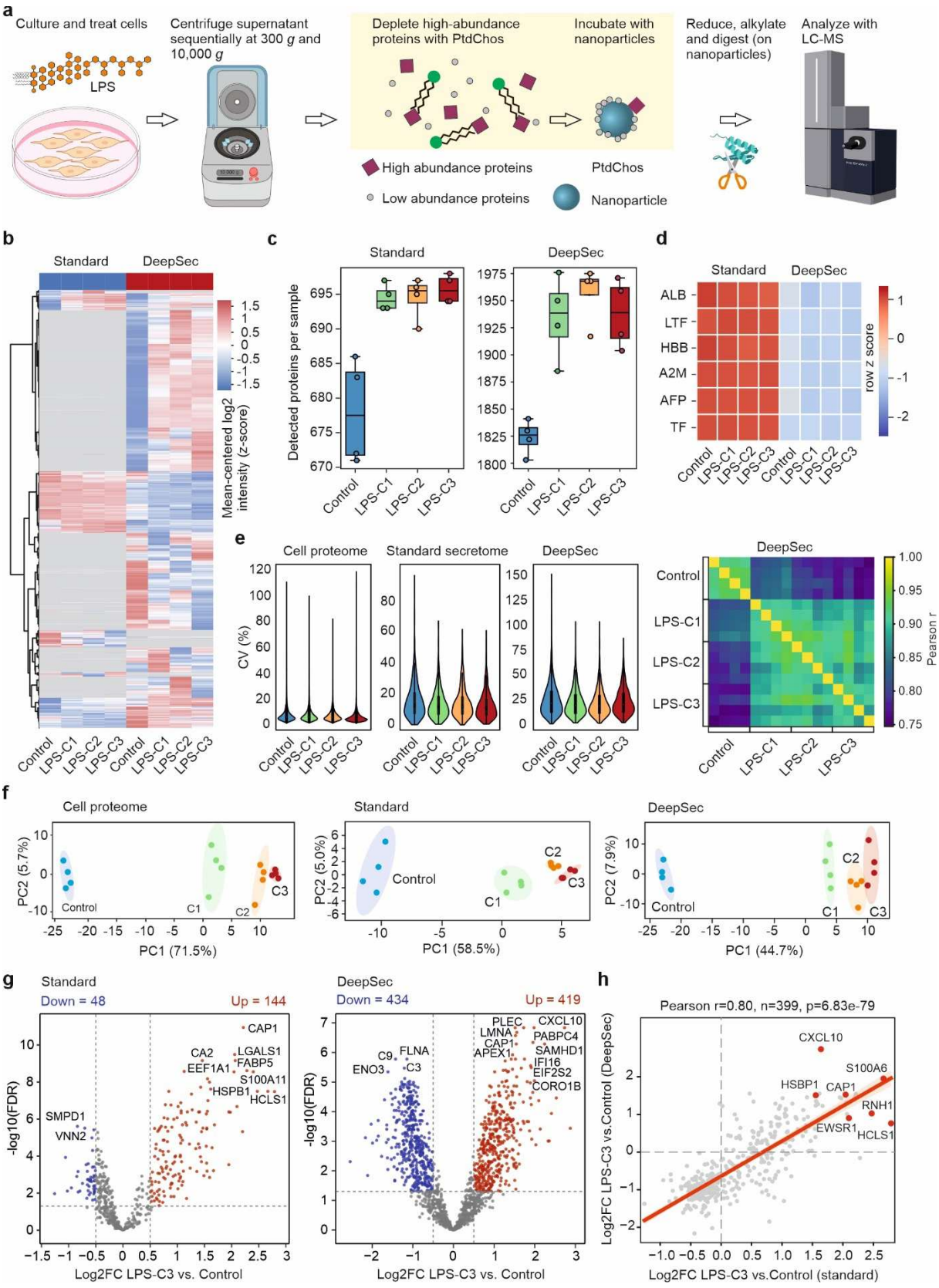


Fig 1. Benchmarking DeepSec against a standard secretome analysis workflow. **a,** Schematic of the secretome analysis workflow. In DeepSec, the section shaded in beige color, represents the small molecule-modulated nanoparticle-based enrichment

step in the workflow. Phosphatidylcholine is used to block albumin and other highly abundant proteins. Subsequently, polystyrene nanoparticles (200 nm, single entity) are used to capture lower abundance proteins. The proteins are then reduced, alkylated and digested on nanoparticles after washing with PBS. **b,** Proteomics profile of secretomes quantified through standard and DeepSec approaches. Missing values are shown in grey. **c,** Number of detected proteins per sample in monocytes treated with vehicle or serial LPS concentrations (C1: 1 ng/ml, C2: 10 ng/ml, C3: 100 ng/ml) using the standard and DeepSec workflows. Detected proteins were defined as proteins with non-zero intensity values in each sample. (Center line—median; box limits contain 50% of data; upper and lower quartiles, 75 and 25%; maximum—greatest value excluding outliers; minimum—least value excluding outliers; outliers—more than 1.5 times of the upper and lower quartiles). **D,** DeepSec depleted the top proteins ranked by their intensity in standard secretome. Z scores in b and d were calculated based on log2-transformed normalized protein intensities and then converted for each protein across all experimental groups. **e,** The CV of analysis in cell proteome, and both secretomes across 4 conditions. Violin plots display the full data distribution as a kernel density estimate mirrored along the vertical axis, with the width indicating the frequency of observations. The center line denotes the median, and box limits within the violin represent the interquartile range (25th–75th percentiles). The Pearson correlation heatmap between replicates in DeepSec is shown. **f,** PCA analysis of normalized log_2 protein intensity profiles across all three datasets. Missing values were imputed prior to PCA. **g,** Overall changes in the secretome upon treatment of monocytes with LPS-C3 (100 ng/ml). Benjamini-Hochberg correction of significance was applied. **h,** Pearson correlation of all shared proteins with a minimum of two peptides across standard and DeepSec approaches at highest LPS concentration as an example. All experiments were performed in four replicates.

In both standard and DeepSec workflows, we observed a concentration-dependent increase in LPS-responsive secreted proteins (**Supplementary Fig 2a-b**). After restricting the analysis to high-confidence quantified proteins used for downstream differential analysis, DeepSec still captured a substantially larger secretome space than the standard workflow. Of the total 1610 proteins robustly quantified in the secretome (>1 peptide), 1105 were exclusively detected by DeepSec (**Fig 2a**), which is due to the capture of low-abundance proteins (**Fig 2b**). DeepSec increased the number of differentially abundant extracellular proteins by 4.4-fold (**Supplementary Fig 2c**). Considering only proteins annotated as secreted in the UniProt (**Supplementary Data 5**), DeepSec delivered 3.8 times more hits compared to the standard workflow (**Fig 2a**). We also illustrate the overlap of the cellular proteome and the secretome profiled by the standard and DeepSec approaches (**Supplementary Fig 2d**).

A breakdown of the significantly secreted proteins showed that DeepSec increased the number of quantified proteins in all categories, while the percentage contribution of each keyword to the secretome remained rather constant (**Fig 2c**). DeepSec provided a higher number of secreted proteins containing a signal peptide, as revealed by SignalP analysis (*20*) (**Fig 2d**). The percentage of SignalP-sequence positive proteins was rather similar in both approaches and slightly higher in DeepSec (**Fig 2e**). The recovery of signal peptide–negative proteins suggests that DeepSec captures extracellular proteins beyond the canonical secretory route, including candidates released through non-classical mechanisms or proteins not yet annotated as secreted,

an observation we explored further through secretion-pathway perturbation experiments.

Clustering of dose-dependent patterns identified several response modes in the standard secretome data, including 45 proteins showing a monotonic increase in abundance (**Fig 2f**), monotonic downregulation, transient induction, transient decrease in abundance, and mixed/other profiles (**Supplementary Fig 2e**). In DeepSec, in addition to monotonic increase in abundance (**Fig 2g**), we observed a large set of transiently induced proteins (n=217), reflecting diverse regulatory mechanisms (**Supplementary Fig 2f**). Pathway analysis of proteins exhibiting monotonic, concentration-dependent responses to LPS treatment revealed significant enrichment of secretory and extracellular pathways in both standard and DeepSec approaches (**Fig 2g**).

We orthogonally validated three LPS-induced targets CXCL10, CXCL8, and IL-1β (the latter only found in DeepSec) by ELISA (**Fig 2h**). Ratios obtained from the ELISA analyses strongly correlated with the DeepSec intensities, with Pearson correlation coefficients ranging from 0.78 to 0.93. Interestingly, IL-1β abundance reached a plateau at 10 ng/mL LPS and decreased at higher LPS concentration in DeepSec. This response pattern was confirmed by ELISA, showing ratios that strongly correlated with DeepSec intensities, thereby validating DeepSec as a robust platform for precise and sensitive secretome analysis able to accurately capture fold changes at a concentration of ~20 pM.

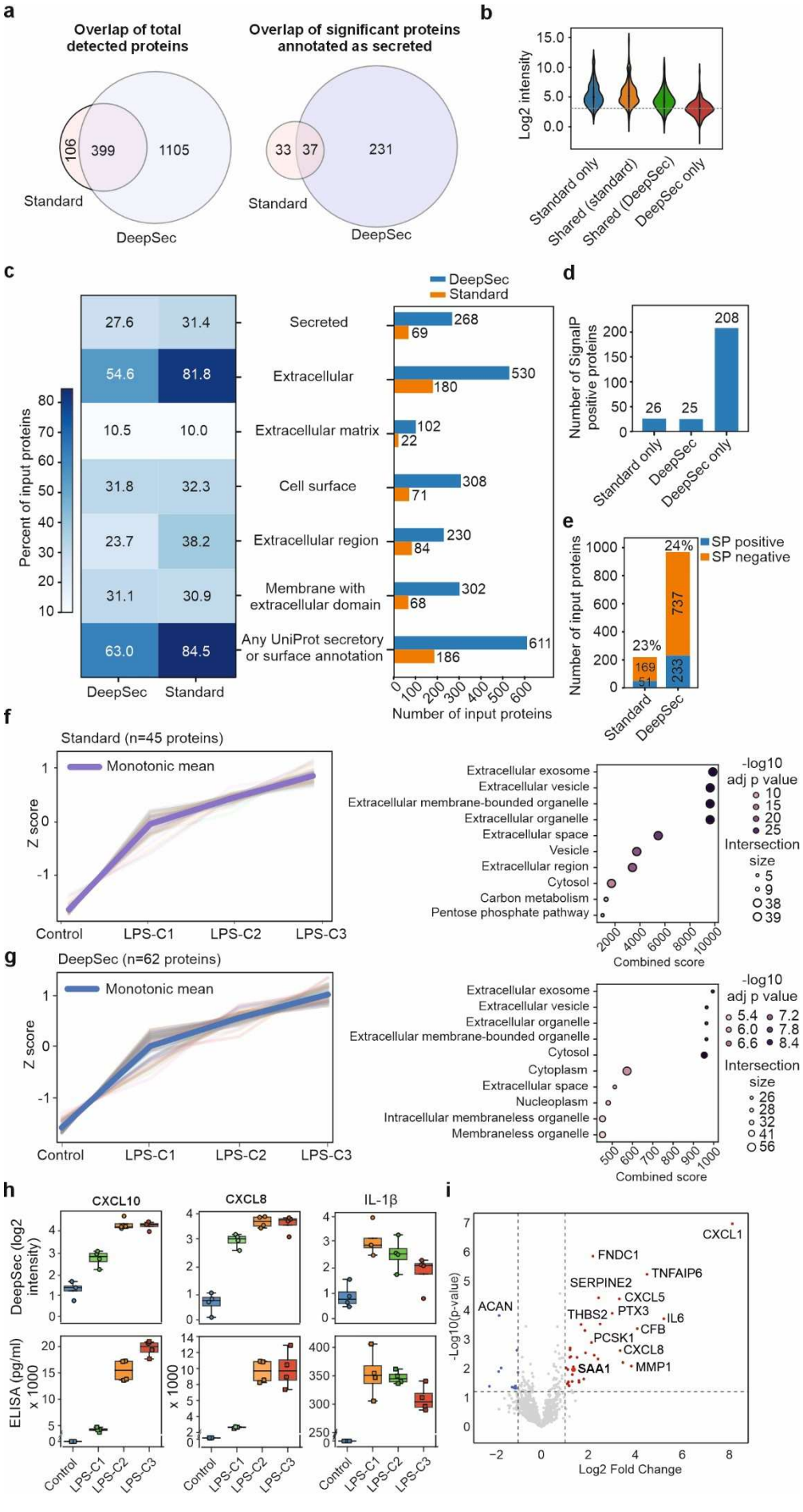

a
Overlap of total detected proteins
106
399
1105
Standard
DeepSec
Overlap of significant proteins annotated as secreted
33
37
231
Standard
DeepSec
b
Log2 intensity
15.0
10.0
5.0
0.0
Standard only
Shared (standard)
Shared (DeepSec)
DeepSec only
c
DeepSec
Standard
Percent of input proteins
27.6
31.4
54.6
81.8
10.5
10.0
31.8
32.3
23.7
38.2
31.1
30.9
63.0
84.5
DeepSec
Standard
Secreted
268
69
Extracellular
530
180
Extracellular matrix
102
22
Cell surface
308
71
Extracellular region
230
84
Membrane with extracellular domain
302
68
Any UniProt secretory or surface annotation
611
186
Number of input proteins
d
Number of SignalP positive proteins
208
26
25
Standard only
DeepSec
DeepSec only
e
Number of input proteins
SP positive
SP negative
24%
737
23%
169
61
233
Standard
DeepSec
f
Standard (n=45 proteins)
Monotonic mean
Z score
Control
LPS-C1
LPS-C2
LPS-C3
Extracellular exosome
Extracellular vesicle
Extracellular membrane-bounded organelle
Extracellular organelle
Extracellular space
Vesicle
Extracellular region
Cytosol
Carbon metabolism
Pentose phosphate pathway
Combined score
-log10 adj p value
Intersection size
g
DeepSec (n=62 proteins)
Monotonic mean
Z score
Control
LPS-C1
LPS-C2
LPS-C3
Extracellular exosome
Extracellular vesicle
Extracellular organelle
Extracellular membrane-bounded organelle
Cytosol
Cytoplasm
Extracellular space
Nucleoplasm
Intracellular membraneless organelle
Membraneless organelle
Combined score
-log10 adj p value
Intersection size
h
CXCL10
CXCL8
IL-1β
DeepSec (log2 intensity)
ELISA (pg/ml) x 1000
Control
LPS-C1
LPS-C2
LPS-C3
i
-Log10(p-value)
Log2 Fold Change
CXCL1
FNDC1
TNFAIP6
SERPINE2
CXCL5
ACAN
THBS2
PTX3
IL6
CFB
PCSK1
CXCL8
SAA1
MMP1

Fig 2. DeepSec expands quantitative secretome coverage and captures validated LPS-responsive extracellular proteins. a, Overlap of all quantified proteins by both approaches, and overlap of significant secreted proteins (based on UniProt) across both approaches. **b,** The distribution of protein intensities detected by standard and DeepSec approaches. Violin plots display the full data distribution as a kernel density estimate mirrored along the vertical axis, with the width indicating the frequency of observations. The center line denotes the median, and box limits within the violin represent the interquartile range (25th–75th percentiles). **c,** The percentage and number of significantly secreted proteins under different UniProt annotations. **d-e,** Number and percentage of significantly altered extracellular proteins predicted to contain an N-terminal signal peptide by SignalP. **f-g**, Number of proteins with monotonic increase in abundance upon increasing LPS concentrations in the standard secretome and the associated pathways in standard and DeepSec. GO cellular component enrichment of monotonic up-regulated proteins from the standard and DeepSec secretomes. Dot size indicates the number of proteins annotated to each term, and dot color represents the FDR. Enrichment was performed against the background of all quantified proteins in the respective dataset. **h**, The trends in the absolute levels of three known LPS-induced targets quantified by ELISA and DeepSec (Boxplot center line—median; box limits contain 50% of data; upper and lower quartiles, 75 and 25%; maximum—greatest value excluding outliers; minimum—least value excluding outliers; outliers—more than 1.5 times of the upper and lower quartiles). ELISA experiments were performed in 4 replicates. **i**, secretome analysis of human adipocytes treated with LPS (log2 fold change=1.31, permutation P value=0.029). All experiments were performed with four replicates.

2.2. DeepSec validates adipocyte SAA1 secretion induced by inflammatory signaling

Having established that DeepSec preserves quantitative accuracy and offers high sensitivity for low-abundance signaling factors, we next sought to evaluate its capability to resolve challenging, cell type-specific secretory events in a complex physiological model. Specifically, we applied the workflow to investigate the inflammatory signaling axis in adipocytes, focusing on targets historically difficult to capture using standard proteomic pipelines.

A recent study identified a distinct adipocyte state enriched in colon-associated visceral fat that is marked by high SAA1/SAA2 expression (*17*). That study combined spatial transcriptomics and single-nucleus RNA sequencing across multiple human adipose depots, showing that epiploic adipose tissue has a unique immune-metabolic organization, characterized by enrichment of SAA-positive adipocytes and immune cells. Mechanistically, they demonstrated that inflammatory stimuli, particularly LPS and TNF-α, induce SAA1 expression in adipocytes and that SAA1 in turn can activate inflammatory programs in adipose-resident myeloid cells, supporting the existence of an adipocyte–immune signaling axis in colon-associated fat. Although these findings established the biological relevance of SAA1 induction in adipocytes, direct detection of secreted SAA1 in conditioned media remains technically challenging. Using DeepSec, we were able to validate SAA1 secretion in LPS-stimulated adipocytes (**Fig 2i**; **Supplementary Data 6**), thereby extending these observations from transcriptional induction to extracellular protein release. In contrast, SAA1 was not detected in a

paired experiment in THP1 cells nor in our other experiments in THP1 cells described above.

2.3. DeepSec characterizes the ER-Golgi and endolysosomal/autophagy-associated secretory pathway in response to LPS

Human cells release proteins through multiple secretory pathways, including the canonical endoplasmic reticulum (ER)-Golgi route as well as alternative mechanisms such as autophagy-mediated and other non-canonical secretion pathways that enable the export of proteins lacking classical signal peptides. To evaluate whether DeepSec resolves pathway contributions to the inflammatory secretome, we pharmacologically inhibited ER-Golgi trafficking or endolysosomal/autophagy-associated vesicle trafficking in LPS-stimulated THP1 cells. These perturbations are expected to prevent pathway-specific protein export, resulting in their intracellular accumulation and depletion in the extracellular secretome.

To inhibit ER-Golgi secretion, we either disrupted ER export using FLI-06 or blocked ER-Golgi vesicular trafficking using brefeldin A (BFA) (**Fig 3a** and **Supplementary Fig 3a**). Interference with endolysosomal trafficking was achieved by targeting autophagy initiation and PI3P-dependent endomembrane dynamics using the ULK1 inhibitor MRT68921 or the VPS34 inhibitor SAR405 (**Fig 3a** and **Supplementary Fig 3b**). In both cases, no measurable loss of membrane integrity or cell viability was observed over the experimental timeframe (**Supplementary Fig 3c**).

Both proteomes and secretomes were analyzed under these conditions (**Supplementary Data 7-8**). The correlation between the replicates and the CVs for DeepSec analysis is shown for the Golgi-ER experiments (**Fig 3b-d**). Upon ER-Golgi perturbation, we identified 81 and 60 proteins significantly reduced in the extracellular secretome while simultaneously accumulated intracellularly in response to LPS combined with FLI-06 or BFA, respectively (**Fig 3e-f**; list of proteins can be found in **Supplementary Data 9**). The higher number of hits for FLI-06 could be related to upstream pathway inhibition. The effects of both inhibitors combined with LPS across the proteome and secretome were highly correlated (**Supplementary Fig 4-5**), supporting a shared blockade of canonical ER-Golgi secretion. Pathway enrichment analysis confirmed strong overrepresentation of proteins annotated to the extracellular space (**Fig 3g**), with the majority of the identified proteins belonging to cytokines/chemokines (CXCL8, CXCL1), growth factors (TGFB2, TGFBI, CCN2, CLEC11A, GDF15, GRN, SEMA7A), extracellular matrix proteins (TIMP1, MMP1, MMP9, MMP14, SDC4, QSOX1, PINLYP, SRGN, APLP2) and innate immune factors (CFD, CST3, PSAP, LTF).

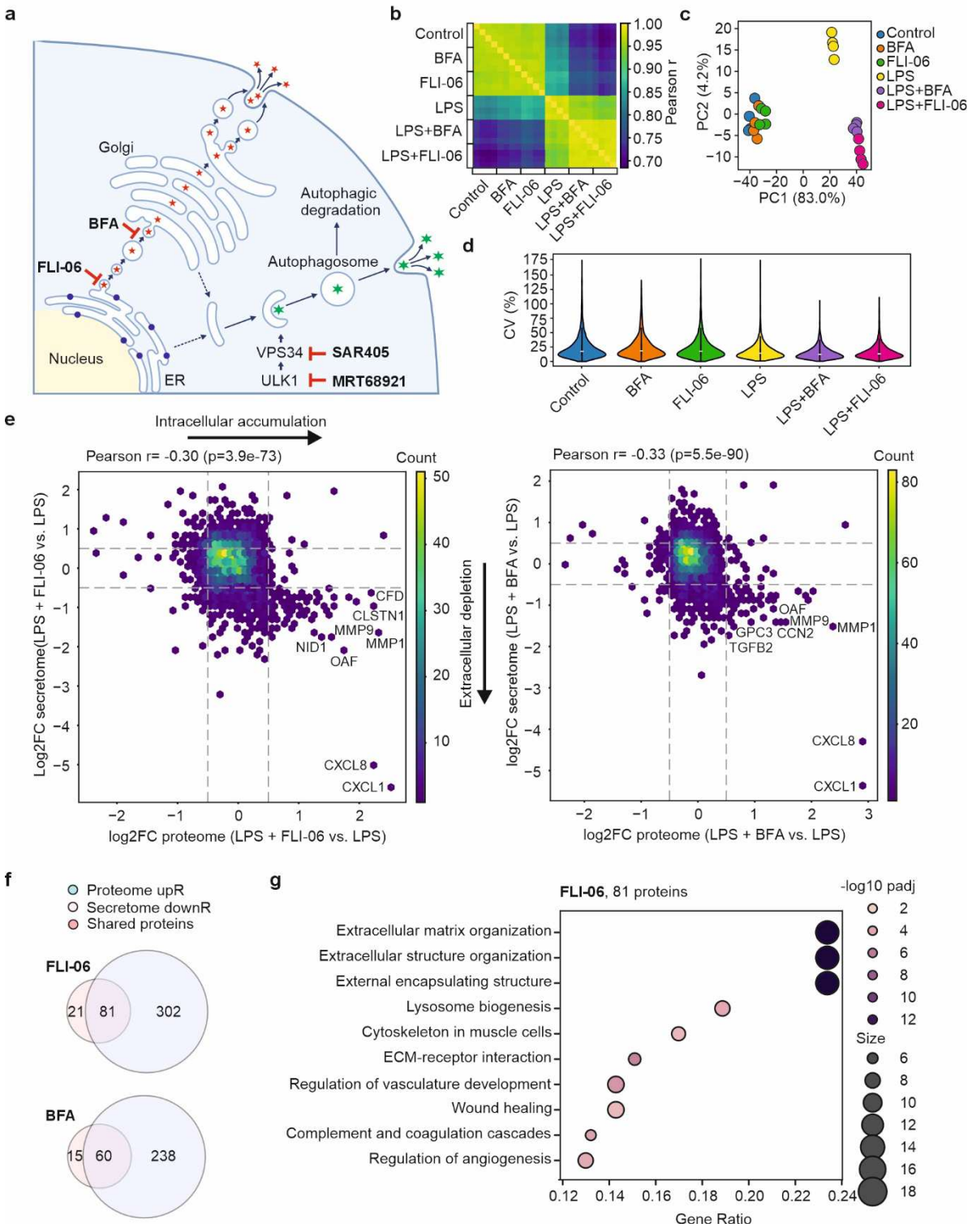


Fig 3. Dissecting the cellular ER-Golgi secretory pathways using DeepSec. a, THP1 cells were stimulated with LPS and treated with specific inhibitors. **b,** Correlations between different replicates. **c,** PCA of DeepSec captured secretomes and the contribution of each treatment to the separations. **d,** CV of the DeepSec analyses. Violin plots display the full data distribution as a kernel density estimate mirrored along the vertical axis, with the width indicating the frequency of observations. The center line denotes the median, and box limits within the violin represent the

interquartile range (25th–75th percentiles). **e,** Hexbin quadrant plots highlight the proteins that are accumulating in the proteome but are depleted in the secretome. **f,** Number of proteins that are upregulated in the proteome and downregulated in the secretomes in response to LPS-FLI-06 vs. LPS alone and LPS-BFA vs. LPS alone. **g,** Enriched pathways for the 81 proteins that are increased in the proteome and decreased in the secretome in response to LPS-FLI-06 vs. LPS alone.

Interference with endolysosomal trafficking resulted in 24 and 17 proteins significantly reduced in the secretome and increased in the intracellular proteome (**Fig 4a-c**; **Supplementary Data 10-11**; list of significant proteins in **Supplementary Data 12**), in response to MRT68921 and SAR405, respectively. Enrichment analysis for the hits for MRT68921 mapped to secretory and extracellular pathways (**Fig 4d**). There was a high overlap of hits between both inhibitors. This subset was composed of classical inflammatory chemokines (CXCL8, CXCL1), complement and immune effectors (C7, C8A, C9, C1QBP, CFI), extracellular matrix and tissue remodeling factors (COL1A1, COMP, LUM, FBLN1, THBS1, MMP1, SERPINF1), and ER-associated quality control proteins (CALR, HSP90B1, PDIA3, PRKCSH, HSPD1). These proteins defined a subset of the inflammatory secretome dependent on endolysosomal/autophagy machinery that was distinct from, but partially overlapping with, the ER-Golgi-dependent secretome.

Interestingly, several of the most strongly induced inflammatory secretory factors, such as CXCL8 and MMP1, exhibited sensitivity to both ER-Golgi disruption and inhibition of VPS34/ULK1-dependent trafficking. Moreover, both CXCL8 and MMP1 accumulated upon lysosomal flux inhibition by Bafilomycin A1 (BafA1), while MMP1 also showed a marked localization to LC3-positive vesicular structures (**Fig 4e-g**). These findings indicate that high secretory demand during macrophage activation is accompanied by engagement of LC3-associated endolysosomal trafficking pathways, which suggests a functional coupling between canonical secretion and autophagic cellular quality control rather than pathway redundancy. This observation is consistent with previous evidence implicating autophagy in the regulation of matrix metalloproteinase secretion (*21*).

Overall, these perturbation experiments demonstrate that DeepSec resolves a pathway-specific LPS-induced inflammatory secretome, distinguishing canonical ER-Golgi-dependent secretion from endolysosomal/autophagy-associated trafficking programs and capturing proteins with shared trafficking dependencies. Consistent with canonical secretion, most identified proteins contained an N-terminal signal peptide across all perturbation-defined secretome subsets (**Fig 4h**). DeepTMHMM topology prediction further indicated that most proteins were classified as signal-peptide-only proteins, with smaller subsets containing transmembrane domains or globular topology (**Fig 4i-j**). Collapsing these predictions into broader secretion-related categories showed that most proteins are classically soluble secreted proteins (**Fig 4k**).

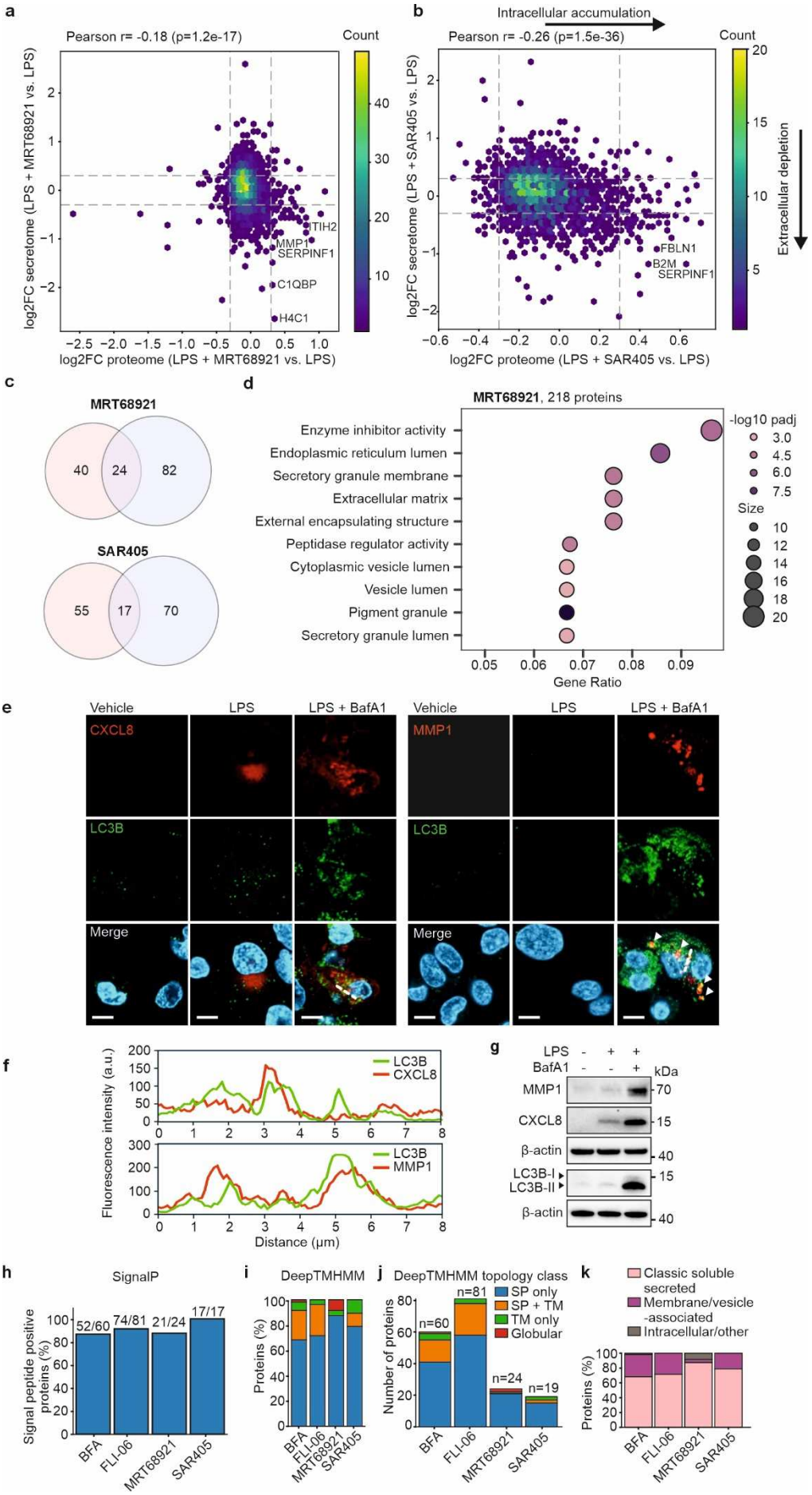

a
Pearson r= -0.18 (p=1.2e-17)
Count
log2FC secretome (LPS + MRT68921 vs. LPS)
log2FC proteome (LPS + MRT68921 vs. LPS)
TIH2
MMP1
SERPINF1
C1QBP
H4C1
b
Intracellular accumulation
Pearson r= -0.26 (p=1.5e-36)
Count
Extracellular depletion
log2FC secretome (LPS + SAR405 vs. LPS)
log2FC proteome (LPS + SAR405 vs. LPS)
FBLN1
B2M
SERPINF1
c
MRT68921
40
24
82
SAR405
55
17
70
d
MRT68921, 218 proteins
Enzyme inhibitor activity
Endoplasmic reticulum lumen
Secretory granule membrane
Extracellular matrix
External encapsulating structure
Peptidase regulator activity
Cytoplasmic vesicle lumen
Vesicle lumen
Pigment granule
Secretory granule lumen
Gene Ratio
-log10 padj
Size
e
Vehicle
LPS
LPS + BafA1
CXCL8
MMP1
LC3B
Merge
f
Fluorescence intensity (a.u.)
LC3B
CXCL8
MMP1
Distance (µm)
g
LPS
BafA1
kDa
MMP1
CXCL8
β-actin
LC3B-I
LC3B-II
h
SignalP
Signal peptide positive proteins (%)
52/60
74/81
21/24
17/17
BFA
FLI-06
MRT68921
SAR405
i
DeepTMHMM
Proteins (%)
j
DeepTMHMM topology class
SP only
SP + TM
TM only
Globular
Number of proteins
n=60
n=81
n=24
n=19
k
Classic soluble secreted
Membrane/vesicle -associated
Intracellular/other
Proteins (%)

Fig 4. Dissecting the endolysosomal/autophagy-associated secretory pathways using DeepSec. a-c, THP1 cells were treated with specific inhibitors and stimulated with LPS. The hexbin quadrant plots highlight the proteins that are accumulating in the proteome but are depleted in the secretome. **d,** Pathway enrichment analysis for the proteins accumulating in the proteome and depleted in the secretome in response to MRT68921 and LPS treatment. **e-g,** Localization of CXCL8 and MMP1 to LC3-positive vesicular structures and their accumulation upon lysosomal flux inhibition by BafA1. **h,** SignalP analysis of the hits discovered using different inhibitors plus LPS. **i-j,** DeepTMHMM topology classification shown as percentages (i) and absolute counts (j). Proteins were classified as signal peptide only (SP only), signal peptide plus transmembrane domain (SP+TM), transmembrane domain only (TM only) or globular. **k,** Collapsed secretion-category annotation based on predicted topology. SP-only proteins were classified as classically secreted soluble proteins; SP + TM and TM-only proteins were classified as membrane/vesicle-associated; globular proteins were classified as intracellular/other.

2.4. DeepSec characterizes dual secretomes in the host-pathogen interface

To evaluate whether DeepSec can simultaneously capture host- and pathogen-derived secreted proteins, we infected human colorectal cancer cell lines SW480 and SW620 cells with key oncogenic pathogen *Fusobacterium nucleatum* under anaerobic conditions for 12 h. DeepSec identified 1,966 and 1,650 human-derived secreted proteins in SW480 and SW620 cells, respectively, as well as 240 and 209 *F. nucleatum*-derived secreted proteins (**Supplementary Data 13**). The change in the secretion of host and bacterial proteins in coculture vs. human cells alone or *F. nucleatum* alone, respectively, is shown in **Fig 5a**. Additionally, we observed a high correlation (Pearson r=0.57) of commonly secreted bacterial proteins in coculture with both human cell lines (**Fig 5b**). Among the most altered bacterial proteins identified in both cocultures was alkyl hydroperoxide reductase subunit C (AhpC) (**Fig 5c**), which protects bacteria against oxygen radicals from the host environment. AhpC has been shown to induce strong antibacterial immune responses during pathogen infection and has been used as an immunogen in mouse models of *F. nucleatum* infection (*22*). Another identified key virulence factor was FomA (FN1859) (**Fig 5c**), one of the most abundant proteins in *Fn* outer membrane vesicles, which is deposited on colorectal cancer cells facilitating bacterial adhesion (*23*), and promoting cancer progression through hyperactivation of ERK/STAT3 signaling pathways (*24*). Interestingly, some other membrane-associated proteins were also identified like the iron transporter FN0375 (only significant in SW620 cells). These might be consistent with release of membrane-associated proteins by encapsulation in outer membrane vesicles (*24*, *25*), but their detection alone does not establish active secretion. After infection, host cells secreted higher levels of proteins related to proliferation like TGFBR3 (*27*), and metabolic rewiring such as PCYOX1L (*28*), both known as extracellular proteins (**Fig 5d**). Importantly, we also noted elevated secretion of ALPL which is commonly increased in CRC metastasis (*29*). Overall, these data show that DeepSec can capture infection-associated remodeling of both bacterial and host extracellular proteomes, revealing candidate mechanisms by which *F. nucleatum* may adapt to the tumor microenvironment and influence colorectal cancer cell behavior.

To directly validate DeepSec's ability to resolve defined bacterial secretion mechanisms in the context of host-microbe interactions, we next infected human cells with enteroaggregative *Escherichia coli* (EAEC) expressing a functional type VI secretion system (T6SS) and isogenic secretion-deficient mutant Δ*tssM* (**Fig 5e**). The

T6SS is a contractile nanomachine conserved among many Gram-negative bacteria and is responsible for the delivery of antibacterial and host-directed effector proteins (*30*). It represents an ideal benchmark system as secretion can be selectively abolished by single-gene deletion without broadly affecting bacterial viability or general protein export.

DeepSec analysis revealed robust detection of canonical T6SS-associated proteins in host cell supernatants infected with wild-type EAEC, including hallmark core components Hcp and VgrG (**Fig 5f-g**; **Supplementary Data 14**). In contrast, these proteins were absent in samples infected with the Δ*tssM* mutant. Notably, the volcano plot revealed reciprocal regulation of T6SS-associated proteins and flagellar components. Multiple flagellar proteins were significantly increased in the Δ*tssM* mutant compared to wild-type EAEC. This inverse relationship between T6SS activity and flagellar assembly has often been reported (*31*) and reflects the opposing functional roles of these systems: while the T6SS promotes interbacterial competition and host interaction, flagella confer motility and chemotaxis. The observed induction of flagellar proteins in the T6SS mutant is therefore fully consistent with established regulatory cross-talk. This experiment demonstrates that DeepSec can identify genetically defined virulence-associated secretion outputs in host-cell supernatants.

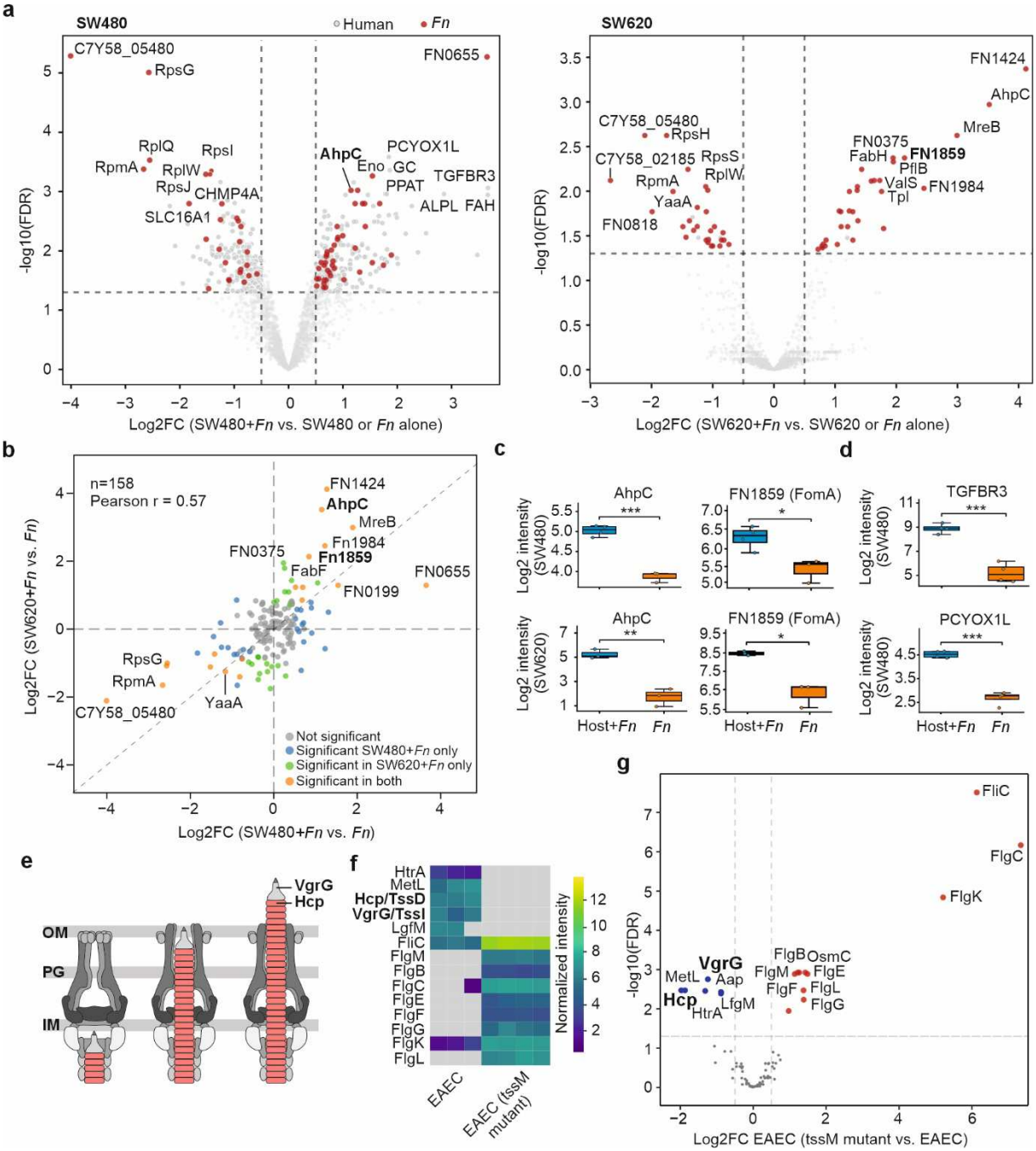


Fig 5. Host-pathogen interaction leads to secretion of host and bacterial proteins. a, The secretory response of human SW480 and SW620 cells and *F. nucleatum* in coculture (host proteins in grey and bacterial proteins are shown in red). **b,** Correlation of proteins found in the secretome of *F. nucleatum* in coculture with human SW480 and SW620 cells. **c,** Exemplary proteins secreted from *F. nucleatum* in coculture with both SW480 and SW620 cells. **d,** Exemplary extracellular proteins secreted from SW480 and SW620 cells in coculture with *F. nucleatum*. (Boxplots in panels c and d: center line—median; box limits contain 50% of data; upper and lower quartiles, 75 and 25%; maximum—greatest value excluding outliers; minimum—least value excluding outliers; outliers—more than 1.5 times of the upper and lower quartiles) **e,** A model of T6SS, highlighting Hcp and VgrG as secretory proteins. **f-g,** The proteins secreted from WT EAEC and Δ*tssM* mutant in coculture with human HCT116 colon

cancer cells. As shown in the heatmap, Hcp and VgrG were not detected in any of the Δ*tssM* mutant replicates.

2.5. DeepSec identifies treatment-response signatures in patient-derived 3D liver microtissues modeling MASH

Finally, we assessed the utility of DeepSec in profiling the secretomes of 3D human liver spheroid model of metabolic dysfunction-associated steatohepatitis (MASH) and its response to therapeutics (*32*). These organotypic cultures, established from primary human hepatocytes (PHH) and non-parenchymal cells from patients with histologically confirmed MASH, recapitulate key pathological features of the disease, including steatosis, inflammation, and fibrosis, and closely align with human biopsy-derived molecular signatures (*32*–*34*). First, we profiled both the intracellular proteome and extracellular secretome of MASH spheroids with high reproducibility (**Supplementary Fig 6a-c**; **Supplementary Data 15-16**). At the phenotypic level, MASH spheroids exhibited a significant increase in hepatic steatosis and fibrosis, which was mirrored at the proteomic level where DeepSec revealed 47 differentially expressed proteins, including an upregulation of perilipins (PLIN1/2/4), apolipoproteins (APOA1/4) and an increase in the expression of HMGCS1 (**Fig 6a**), aligning with molecular changes observed in MASH patient livers. The lipid content and pro-collagen Iα1 analyses corroborated the model (**Fig 6b-c**). Titration of non-parenchymal cell types showed that the addition of Kupffer cells (KCs) resulted in a drastic upregulation of its *bona fide* markers CD163 and GAS6, as well as various complement components (C1QA, C1QC) (**Fig 6d-e**). Similarly, addition of hepatic stellate cells (SCs) resulted in significantly elevated levels of HSC markers (ACTA2, PDGFRB, TIMP1, SERPINE1, and LOX) and the broad induction of extracellular matrix (ECM) proteins (COL1A1/2, FBN1, DCN, TNC and LAMB1) (**Fig 6d,f**). Analysis of MASH spheroid secretomes demonstrated significant increases in 105 proteins, including augmented apolipoprotein secretion (**Fig 6g**), as well as release of ENPP2 and PCSK9, which are adversely associated with systemic metabolic risk. The enriched pathways generally mapped to wound healing, lipid transport and processing and other extracellular terms (**Supplementary Fig 6d**).

Next, we evaluated whether pharmacological treatment could revert these effects (the volcano plots for both proteomes and secretomes are depicted in **Supplementary Fig 6e-f**). Phenotypically, we observed a moderate decrease in hepatic steatosis and fibrosis upon exposure of MASH spheroids with the triple GLP-1R/GIPR/GCGR agonist retatrutide or the approved THRβ agonist resmetirom, whereas the pan-PPAR agonist lanifibranor had only mild effects (**Fig 6h-j**). At the proteome level, we calculated a steatosis-associated protein score based on 10 lipid droplet-, fatty acid uptake-, and lipid metabolism-related proteins, which showed treatment-dependent changes consistent with the triglyceride accumulation phenotype (**Fig 6k**). Cell Painting for reactive oxygen species further showed that these improvements were paralleled by an overall reduction in oxidative stress (**Fig 6l**). Similar effects were observed at the level of fibrosis where resmetirom reduced pro-collagen Iα1 levels (**Fig 6m**). This effect was further amplified when considering a list of fibrotic proteins differentially expressed in MASH and resolved via DeepSec, providing additional mechanistic resolution (**Fig 6n**).

We then cross-referenced these responses with treatment-associated changes in proteomic signatures and extracellular signaling output to identify convergent and drug-specific mechanisms underlying therapeutic modulation of MASH in patient-derived cells. Critically, treatment with lanifibranor, retatrutide and resmetirom reversed these alterations and induced a rewiring of metabolic processes in the cell proteome, evidenced by an upregulation of PCK1 and ACSS1 (**Fig 6o**), key metabolic regulators commonly downregulated in MASH. Most similarities were observed between resmetirom and retatrutide, which both resulted in a significant downregulation of the gatekeepers of hepatic lipid flux (HMGCS1 and GCK) (**Fig 6o**). Furthermore, resmetirom inhibited collagens (COL1A1 and COL2A1) and IL18 (**Supplementary Fig 6g**). In contrast, lanifibranor showed a distinctly different signature limited to metabolic alterations, comprising the fatty acid translocase CD36, as well as proteins involved in fatty acid and lipid handling, such as FABP4 and PLIN4, without apparent impact on ECM remodeling or fibrosis (**Supplementary Fig 6h**). To demonstrate the broad effect of the drugs on the proteome and secretome of MASH spheroids, we plotted the expression of the 30 top proteins across the proteome and secretome (**Fig 6p**). Retatrutide and resmetirom could reverse the expression of many signature proteins, while lanifibranor had weaker and, at times, opposite effects. Combined, these results showcase the potential of DeepSec to profile both intracellular proteomes and secretomes of patient-derived microtissues with limited inputs and reveal differences in the molecular networks impacted by clinical candidates for MASH.

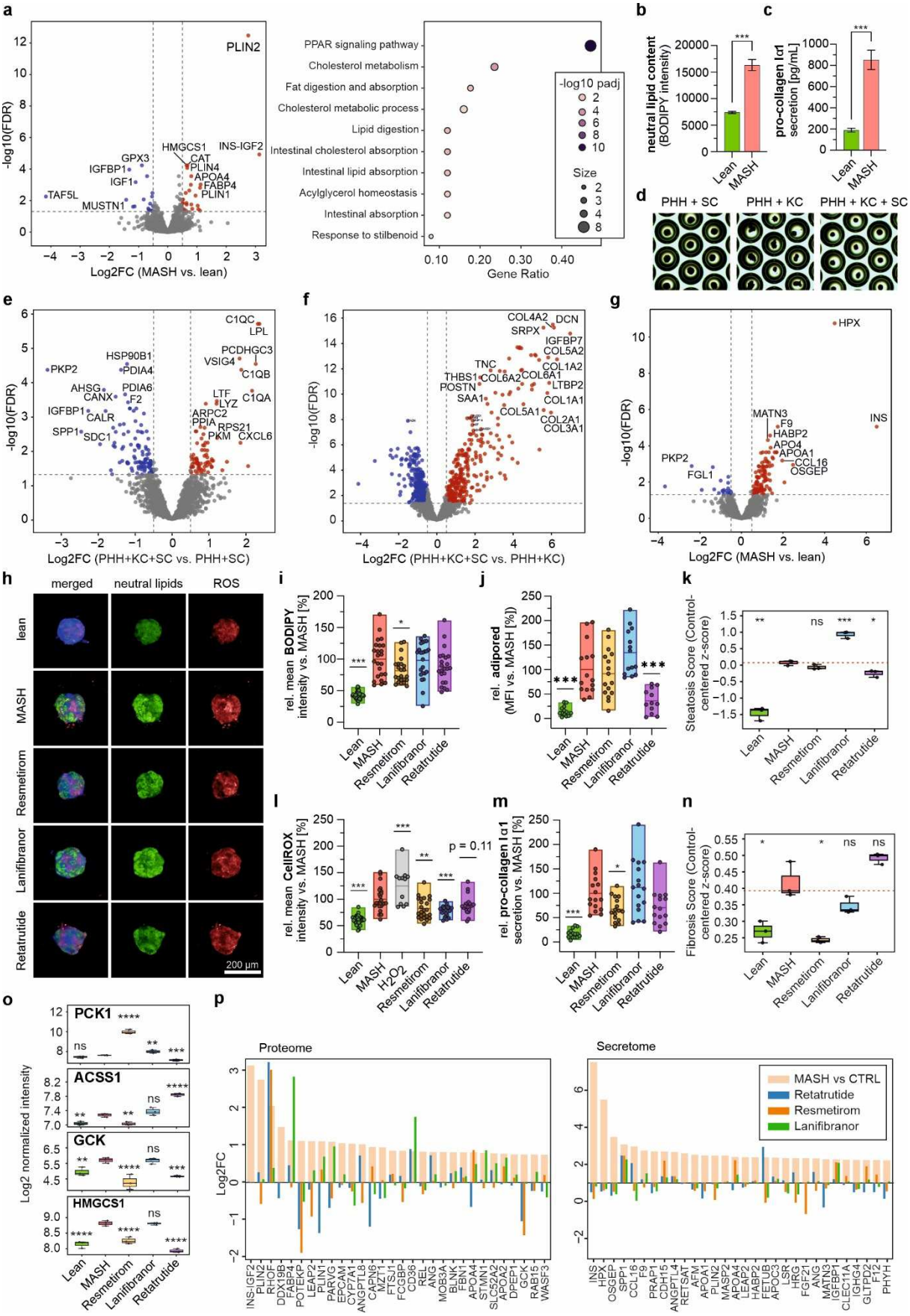

a
PLIN2
-log10(FDR)
Log2FC (MASH vs. lean)
HMGCS1
INS-IGF2
CAT
PLIN4
APOA4
FABP4
PLIN1
GPX3
IGFBP1
IGF1
TAF5L
MUSTN1
PPAR signaling pathway
Cholesterol metabolism
Fat digestion and absorption
Cholesterol metabolic process
Lipid digestion
Intestinal cholesterol absorption
Intestinal lipid absorption
Acylglycerol homeostasis
Intestinal absorption
Response to stilbenoid
-log10 padj
Size
Gene Ratio
b
neutral lipid content (BODIPY intensity)
Lean
MASH
c
pro-collagen Iα1 secretion [pg/mL]
d
PHH + SC
PHH + KC
PHH + KC + SC
e
Log2FC (PHH+KC+SC vs. PHH+SC)
C1QC
LPL
PCDHGC3
VSIG4
C1QB
C1QA
HSP90B1
PDIA4
PKP2
AHSG
CANX
PDIA6
F2
LTF
LYZ
IGFBP1
CALR
ARPC2
PPIA
RPS21
PKM
CXCL6
SPP1
SDC1
f
Log2FC (PHH+KC+SC vs. PHH+KC)
COL4A2
DCN
SRPX
IGFBP7
COL5A2
COL1A2
TNC
THBS1
COL6A2
COL6A1
POSTN
SAA1
LTBP2
COL1A1
COL5A1
COL2A1
COL3A1
g
Log2FC (MASH vs. lean)
HPX
MATN3
F9
HABP2
APO4
APOA1
CCL16
OSGEP
INS
PKP2
FGL1
h
merged
neutral lipids
ROS
lean
MASH
Resmetirom
Lanifibranor
Retatrutide
200 µm
i
rel. mean BODIPY intensity vs. MASH [%]
j
rel. adipored (MFI vs. MASH [%])
k
Steatosis Score (Control-centered z-score)
l
rel. mean CellROX intensity vs. MASH [%]
p = 0.11
m
rel. pro-collagen Iα1 secretion vs. MASH [%]
n
Fibrosis Score (Control-centered z-score)
o
Log2 normalized intensity
PCK1
ACSS1
GCK
HMGCS1
p
Proteome
Secretome
Log2FC
MASH vs CTRL
Retatrutide
Resmetirom
Lanifibranor

Fig 6. DeepSec resolves disease- and treatment-associated proteomic changes in patient-derived 3D MASH liver spheroids. MASH spheroids were generated from primary human hepatocytes (PHH) and non-parenchymal cells, and treated with lanifibranor, retatrutide or resmetirom. **a,** DeepSec identified 47 significantly altered proteins, including increased abundance of perilipins (PLIN1, PLIN2 and PLIN4), apolipoproteins (APOA1 and APOA4) and HMGCS1, consistent with molecular alterations observed in human MASH. Pathways enriched for top 27 upregulated proteins are shown. **b-c,** Measurement of neutral lipids and pro-collagen Iα1 levels in MASH vs. lean spheroids. **d,** Microscopy images of co- and triple-culture spheroids comprising PHH, Kupffer cells (KC) and Stellate cells (SC). **e-f,** Proteomic effects of titrating non-parenchymal cell populations. Addition of KCs increased the abundance of CD163, GAS6 and complement components, including C1QA and C1QC (**e**), whereas addition of hepatic stellate cells induced stellate-cell and fibrosis-associated proteins, including ACTA2, PDGFRB, TIMP1, SERPINE1 and LOX, together with extracellular-matrix proteins such as COL1A1, COL1A2, FBN1, DCN, TNC and LAMB1 (**f**). **g,** Differential secretome analysis identified 105 proteins significantly increased in MASH spheroids, including apolipoproteins and the systemic metabolic-risk-associated proteins ENPP2 and PCSK9. **h,** Representative Cell Painting images of hepatic steatosis and reactive oxygen species in control and MASH spheroids, with or without pharmacological treatment (referring to quantifications in **i** and **l**). **i-j** Quantification of lipid content by BODIPY neutral lipid staining (**i**) and AdipoRed fluorescence intensity (**j**) in the liver spheroids with and without drugs. **k,** Proteomics-derived steatosis scores in lean, MASH, and drug-treated MASH spheroids. Scores were calculated as mean control-centered z-scores of predefined protein signatures. The steatosis signature included PLIN1, PLIN2, PLIN4, CD36, FABP4, HMGCS1, APOA1, APOA4, ANGPTL8, and ME1. **l-m,** Measurement of oxidative stress by ROS staining, (CellROX, **l**) and fibrosis via pro-collagen Iα1 secretion (**m**) in the spheroids and in response to drugs. H_2O_2 serves as positive control for ROS. **n,** Proteomics-derived fibrosis scores in lean, MASH, and drug-treated MASH spheroids. Scores were calculated as mean control-centred z-scores of predefined protein signatures. The fibrosis signature included TAGLN, PDGFRB, FAP, COL1A1, COL1A2, COL3A1, COL6A1, COL6A2, COL6A3, LOX, TIMP1, SERPINE1, SPARC, FN1, DCN, LAMB1, FBN1, and BGN. **o,** Treatment-associated changes in intracellular protein signatures. Lanifibranor and retatrutide increased protein levels of the metabolic regulators PCK1 and ACSS1. Resmetirom and retatrutide produced similar signatures characterized by reduced abundance of proteins controlling hepatic lipid flux and lipid-droplet handling, including GCK and HMGCS1. **p**, The overall changes in the top 30 upregulated proteins in the proteome and secretome of the MASH model and their respective changes in response to the drugs. The proteome and secretome analyses were performed in four replicates. For non-proteomics analyses, data are presented as [mean ± s.d./s.e.m.]; *n* = 12-39 independent spheroid preparations. Statistical significance was determined using ANOVA. *, **, *** indicate $p<0.05$, $p<0.01$ and $p<0.001$, respectively.

3. Discussion

DeepSec establishes small-molecule–modulated protein corona engineering as a quantitative sample-preparation strategy for secretome proteomics. Secreted proteins are central mediators of cell–cell communication, but their discovery by MS is hampered by the dynamic range imposed by serum-containing culture media. By selectively reducing the contribution of bovine albumin and other abundant medium-derived proteins, DeepSec substantially expands secretome depth while preserving the physiological advantages of serum-containing culture. Historically, the majority of secretomics experiments have been performed in serum-free culture conditions, which often stress cells, suppress proliferation, and induce cell death, ultimately causing contamination. Across inflammatory macrophages, adipocytes, host–pathogen cocultures and patient-derived liver microtissues, this approach increased access to low-abundance extracellular proteins and enabled discovery of biological signals that were poorly captured, or missed entirely, by standard workflows. Beyond MS–based proteomics, this depletion strategy can be applied upstream of ELISA and proximity extension assays (e.g., Olink) to remove abundant proteins and enable the analysis of secretome and other biological fluids.

A central advance of this study is the demonstration that protein-corona-based enrichment can preserve quantitative biological differences. Protein corona workflows have previously been developed primarily for depth, throughput and reproducibility, with quantitative performance commonly evaluated using controlled spike-in or cross-species matrix-mixing experiments (*35*). Although these designs are useful for defining analytical linearity, they do not fully capture the complexity of endogenous biological regulation, where proteins change over broad concentration ranges, pathway dependencies and secretion kinetics. Here, DeepSec preserved LPS-induced fold changes relative to a standard secretome workflow and showed strong agreement with orthogonal ELISA measurements for CXCL8, CXCL10 and IL-1β. This provides, to our knowledge, the first demonstration that a protein-corona enrichment workflow can quantitatively track endogenous proteomic changes across a real biological perturbation series. Thus, DeepSec is not simply an enrichment strategy; it is a quantitative technology for measuring dynamic extracellular biology.

This distinction is important because enrichment-based proteomics can distort relative protein abundance if capture is strongly biased by competition, affinity saturation or matrix effects. The preservation of biological fold changes by DeepSec suggests that small-molecule modulation of nanoparticle–protein interactions can compress sample complexity without erasing condition-dependent quantitative information. The observation that DeepSec captured IL-1β at low abundance and reproduced its non-linear dose response by ELISA further illustrates that the method can recover biologically meaningful secretion patterns near the lower limits of conventional secretome proteomics. Similarly, detection of adipocyte-derived SAA1 after LPS stimulation extends transcriptomic evidence of inflammatory adipocyte states (*17*) to direct extracellular protein release. These examples highlight how DeepSec can bridge predicted intercellular communication from transcriptomics with direct proteomic evidence of secreted mediators.

DeepSec also enables mechanistic analysis of secretion pathways when combined with paired intracellular proteome measurements. Perturbation of ER–Golgi trafficking identified proteins that accumulated intracellularly while being depleted from the extracellular compartment, consistent with blockade of canonical secretion. In parallel,

inhibition of ULK1- and VPS34-dependent trafficking resolved an endolysosomal/autophagy-associated component of the inflammatory secretome. The partial overlap between these classes, including proteins such as CXCL8 and MMP1, suggests that inflammatory secretion is not organized into strictly independent canonical and non-canonical routes. Rather, high secretory demand during macrophage activation may couple ER–Golgi transport to endolysosomal and autophagy-associated membrane dynamics. In this context, DeepSec provides a quantitative framework for assigning secreted proteins to trafficking dependencies based on coordinated intracellular accumulation and extracellular depletion.

The host–pathogen experiments extend the utility of DeepSec to mixed-species extracellular proteomics. In colorectal cancer cell cocultures with *F. nucleatum*, DeepSec simultaneously detected host- and bacterium-derived proteins, providing a proteomic view of the extracellular host–microbe interface. Detection of bacterial proteins such as AhpC is consistent with bacterial adaptation to host-associated stress. The experiment on the EAEC type VI secretion system provides an important genetically defined benchmark for bacterial secretion. Detection of canonical T6SS components, including Hcp and VgrG, in wild-type infection and their loss in the secretion-deficient Δ*tssM* mutant demonstrates that DeepSec can resolve *bona fide* secretion-system-dependent bacterial proteins in host cell supernatants. This experiment strengthens the conclusion that the method is sensitive not only to bulk extracellular protein release but also to specific virulence-associated secretion mechanisms. The reciprocal increase in flagellar proteins in the Δ*tssM* mutant further illustrates how DeepSec can capture broader extracellular remodeling associated with bacterial regulatory states.

Finally, the experiments on patient-derived 3D liver microtissues modeling MASH demonstrate the translational value of DeepSec for complex human disease models. In 3D liver microtissues containing primary hepatocytes and non-parenchymal cells, DeepSec captured disease-associated extracellular remodeling, including increased apolipoproteins, metabolic-risk-associated factors and extracellular matrix proteins. When combined with intracellular proteomics and phenotypic readouts, the secretome revealed treatment-specific responses to retatrutide, resmetirom and lanifibranor. Retatrutide and resmetirom produced broader reversal of MASH-associated lipid, oxidative stress and fibrosis signatures, whereas lanifibranor showed a more restricted metabolic response. These data illustrate how deep secretome profiling can complement cellular proteomics to resolve drug-specific mechanisms in patient-derived systems. The application of this tool on spheroids established from various individuals can help monitor therapeutic response to drugs *ex vivo*.

To reduce contamination from intracellular proteins, we used two-step centrifugation to sequentially remove floating cells and debris. In contrast, a single high-speed spin can rupture cells, release intracellular proteins, and increase sample heterogeneity, likely contributing to the reproducibility challenges historically associated with secretome analysis. It should be considered that DeepSec enriches a broad extracellular proteome but is unlikely to capture every secreted protein equally. Recovery may depend on abundance, physicochemical properties, post-translational modifications, complex formation, and competitive adsorption to the nanoparticle surface. Detection of intracellular or membrane-associated proteins in extracellular fractions also requires cautious biological interpretation, particularly in infection, stress-response and long-term culture models. Thus, DeepSec should be paired with viability assessment, appropriate centrifugation or filtration controls, intracellular proteome comparison and

targeted validation when assigning proteins to active secretion routes. In addition, while the current workflow performed robustly across diverse models, nanoparticle chemistry, small-molecule adjuvants and input conditions may require further optimization for additional matrices, organisms and clinical applications.

In summary, DeepSec provides a quantitative protein-corona-based platform for deep secretome proteomics in biologically relevant culture systems. By combining increased depth with preservation of endogenous fold changes, DeepSec addresses a central limitation of conventional secretome workflows and previous protein-corona proteomics applications. Its ability to profile low-abundance cytokines, pathway-dependent secretory programs, mixed host–pathogen extracellular proteomes and drug-response signatures in patient-derived microtissues positions DeepSec as a broadly applicable technology for studying extracellular communication in disease models and therapeutic-response systems.

Online Methods

Cell culture and treatments

THP1 cells and LPS: THP1 human monocytic cells (ATCC, TIB-202) were cultured in RPMI-1640 medium (Cytiva, SH30027.01) supplemented with 10% FBS (Gibco, A5256801) under standard conditions (37°C, 5% CO2). For each experimental condition, 1 x 10^6 THP1 cells were seeded in 6 well plates and differentiated into macrophages by treatment with 20 ng/mL phorbol 12-myristate 13-acetate (PMA; Sigma-Aldrich, P8139) for 24 h, followed by 24 h rest in PMA-free medium prior to stimulation. Cells were then stimulated with 1, 10 or 100 ng/mL of purified *Klebsiella pneumoniae* LPS (Sigma-Aldrich, L4268) for 8 h (n = 4 per condition). For secretory pathway perturbation experiments, THP1 cells were pretreated with 5 µg/mL Brefeldin A (Sigma), 10 µM FLI-06 (Sigma), 1 µM SAR405 (Sigma) or 1 µM MRT68921 (Sigma), for 15 min before stimulation with 10 ng/mL LPS for 6 h. To inhibit the autophagic flux, 0.1 µM bafilomycin A1 (Sigma) was added to the cells 30 min before the treatment. Following treatment, cell culture supernatants were collected, sequentially centrifuged at 300 g for 5 min (to remove floating cells) and at 10,000 g for 10 min (to remove cell debris). In parallel, adherent cells were lysed in denaturing buffer (8 M urea, 1% SDS, 50 mM Tris pH 8.5) supplemented with Halt protease inhibitor cocktail (Thermo Fisher Scientific, #78429).

Adipose-Derived Progenitor Cell Culture for Secretome Analysis: Adipose-derived progenitor cells were isolated from subcutaneous white adipose tissue of one anonymous male donor. Cells were maintained under standard culture conditions (37 °C, 5% CO_2, humidified incubator) in a proliferation medium consisting of DMEM (31885-023, Gibco) supplemented with 10 mM HEPES (15630-056, Gibco), 10% fetal bovine serum (FBS; SV30160, Hyclone), 50 µg/mL Penicillin-Streptomycin (15140-122, Gibco), and 2.5 ng/mL fibroblast growth factor 2 (FGF2; F0291, Sigma-Aldrich). Upon reaching confluence, cells were maintained for an additional three days before FGF2 withdrawal. Adipogenic differentiation was induced the following day using a 1:1 (v/v) mixture of DMEM and Ham's F12 (21765-037, Gibco) containing 5 µg/mL insulin (I9278, Sigma-Aldrich), 1 µM dexamethasone (D1756, Sigma-Aldrich), 100 µM 3-isobutyl-1-methylxanthine (IBMX; I5879, Sigma-Aldrich), 0.2 nM 3,3',5-triiodo-L-thyronine (T6397, Sigma-Aldrich), 10 µg/mL transferrin (T8158, Sigma-Aldrich), and 10 µM rosiglitazone (71740, Cayman Chemicals) for 3 days. Dexamethasone and IBMX were subsequently removed from the medium, followed by rosiglitazone removal

at day 10. Fully differentiated adipocytes were used 12 days post-induction. For secretome collection, cells were incubated for 24 h in medium supplemented with 1% FBS and either 10 ng/mL LPS (O55:B5; L4524, Sigma-Aldrich) or sterile distilled water as a vehicle control.

Following the 24-hour stimulation period, conditioned media were collected and subjected to sequential centrifugation steps at 4 °C: first at 100 × g for 3 minutes, after which 80 µL was carefully removed from the top layer to eliminate residual floating cells, followed by centrifugation at 10,000 × g for 10 minutes. The resulting supernatants were transferred to fresh tubes and snap-frozen at −80 °C until secretome analysis.

Infection of SW480 and SW620 cells with F. nucleatum: Colorectal SW480 and SW620 cells were cultured in RPMI 1640 Glutamax (Gibco) supplemented with 10% FBS (Sigma), penicillin/streptomycin (50 U/ml, Cytivia) in 37°C, 5% CO_2. The day before the experiment, cells were seeded in medium without antibiotics supplemented with 10% FBS at 3.5 x 10^5 cells/well in 6 well plates. Next day, cells were infected with *F. nucleatum subsp. animalis* at MOI=100 for 12h in anaerobic conditions using anaerobic chamber (Whiteley A20, Don Whiteley Scientific). For this experiment bacteria were prepared as follows: *F. nucleatum subsp. animalis* DSM19679 were grown anaerobically for 7 days on blood agar plates: brain-heart infusion (BHI, Becton-Dickinson) with addition of yeast extract containing 0.5 mg/mL L-cysteine, 10 µg/mL hemin, 0.5 µg/mL vitamin K. Two days prior to infection bacteria were inoculated into liquid BHI (with addition of above supplements without blood) and kept for around 20h anaerobically. Next day, a new bacterial liquid culture was prepared at OD_{600}=0.1 and kept again for around 20 h anaerobically. At the day of infection, bacteria were spun down (15 min, 4°C, 3250 x g), bacterial supernatant was aspirated, and the bacterial pellet was washed once with PBS. Bacterial suspensions at OD_{600}=1 (corresponding to 5 x 10^8) prepared in PBS were used for infection. To study secreted proteins released by bacteria alone, the same volume of bacteria as those used to infect cells was added to the wells with cell media only and incubated in anaerobic conditions.

HCT116 cells and E. coli: Human colorectal carcinoma HCT116 cells were cultured in DMEM (Gibco, 42430) supplemented with 10% fetal bovine serum (FBS; Gibco, 10270106) and penicillin–streptomycin (Sigma-Aldrich, P4333) at 37 °C with 5% CO_2. Cells were seeded at 8 × 10^5 cells per 60-mm dish and infected 24 h later. Enteroaggregative *E. coli* (EAEC) wild-type and the T6SS-deficient Δ*tssM* mutant were added to HCT116 cells at a multiplicity of infection (MOI) of 50. Infections were carried out for 4 h at 37 °C. Experiments were performed with four biological replicates per condition, including: (1) EAEC alone, (2) EAEC Δ*tssM* alone, (3) HCT116 cells alone, (4) HCT116 cells infected with EAEC, and (5) HCT116 cells infected with EAEC Δ*tssM*. The collected supernatants were sequentially centrifuged to remove host cells and bacteria, and filtered through 0.45 µm filters (Sarstedt, 83.1826) to ensure sterility. Absence of viable bacteria in filtered supernatants was confirmed by plating on LB agar.

Spheroid culture: Primary human liver spheroids were cultured as described previously (*33*) with relevant modifications detailed below. Primary human hepatocytes (PHH), primary human stellate cells (SC), and primary human Kupffer cells (KC) were commercially acquired from BioIVT (Westbury, NY, USA) and LifeNet Health (San Diego, CA, USA) (donor information is given in **Supplementary Table 1**). Liver cells were seeded into multiplexing 96-well plates (Elplasia #4442, Corning) in William's E

medium supplemented with 11 mM glucose, 100 nM dexamethasone, 5.5 mg/L transferrin, 6.7 µg/L selenite, 2 mM L-glutamine, 100 U /mL penicillin, 0.1 mg/mL streptomycin, and 10% fetal bovine serum (FBS). Insulin was added at 10 ng/mL (control) or 10 µg/mL (MASH condition). Three different cell compositions were used: PHH:KC:SC at 6:1.5:1 ratio (56,667 cells total), PHH:KC at 6:1.5 ratio (50,000 cells total), and PHH:SC at 6:1 (46,667 cells total). Following spheroid formation (5 days post-seeding), FBS was phased out and medium was replaced with albumin-conjugated free fatty acids (FFA; 240 µM palmitic acid and 240 µM oleic acid) or the equivalent amount of unconjugated albumin (control), together with test compounds at 0.1% DMSO (v/v). Medium was changed every 2–3 days and supernatant was collected at every media change by pooling the supernatant from 10 wells per replicate in protein low binding tubes. Subsequently, the supernatant cleared by sequential centrifugation (500 ×g, 5 min; 10,000 ×g, 5 min) to remove cell debris, and stored at −80 °C. On day 7, spheroids were collected in 100 µL PBS per well, pelleted at 500 ×g for 5 min, and stored at −80°C. All work was conducted under ethical permit 2024-05808-01 (Etikprövningsmyndigheten, Sweden).

Supplementary Table 1. Medical and demographic information of liver cell donors.

	Source	Identifier	Sex	Age	Ethnicity	BMI	Medical History/ Cause of Death	Medi-cation	NAS score	Fibrosis stage
Primary human hepato-cytes	BioIVT	AZG	F	40	Hispanic	25.3	Hypertension, Type II Diabetes, prior CVA, Toxoplasmosis positive Anoxia/ Head Trauma	insulin	N/A	N/A
Primary human hepato-cytes	BioIVT	IIN	F	57	Cau-casian	21.3	Hypertension, cholecystectomy, ovary removed, shoulder replacement, Toxoplasmosis negative Anoxia / Cardiovascular	Lisinopril, pain medi-cation	N/A	N/A
Primary stellate & Kupffer cells	LifeNet Health	2111451	F	45	Hispanic	32.0	Anoxia	-	5	1a

Proteomics sample preparation

Cell proteomes (DDA): For the cell proteome analysis, according to our previous protocol (*36*), the cell lysates were subjected to 1 min sonication using a Branson probe sonicator with 3 s on/off pulses and a 30% amplitude. Protein concentration was measured using Pierce BCA Protein Assay Kit (Thermo), and the volume corresponding to 30 µg of protein was transferred from each sample to new tubes. DTT was added to a final concentration of 10 mM and samples were incubated for 45 min at room temperature (RT). Subsequently, IAA was added to a final concentration of 50 mM and samples were incubated at RT for 1 h in the dark. The reaction was quenched by adding an additional 10 mM of DTT. Proteins were precipitated by methanol/chloroform and resuspended in 20 mM EPPS buffer pH 8.5 with 8 M urea. Urea was diluted to 4 M by adding 20 mM EPPS. Lysyl endopeptidase (LysC; Thermo)

was added at a 1:75 w/w ratio to protein and incubated at RT overnight. Samples were diluted with 20 mM EPPS to the final urea concentration of 1 M, and trypsin was added at a 1:75 w/w ratio to protein, followed by incubation for 6 h at RT.

Acetonitrile (ACN) was added to a final concentration of 20% and TMTpro-16plex reagents were added 4× by weight (200 µg) to each sample, followed by incubation for 2 h at RT. The reaction was quenched by the addition of 0.5% hydroxylamine. Samples within each replicate were combined, acidified by TFA, cleaned using Sep-Pak cartridges (Waters), and dried using DNA 120 SpeedVac Concentrator (Thermo). TMT-labeled peptides were fractionated by high-pH reversed phase separation using a XBridge Peptide BEH C18 column (3.5 µm, 130 Å, 1 mm x 150 mm, Waters) on an Ultimate 3000 system (Thermo Scientific). Peptides were loaded on column in buffer A and the system was run at a flow of 42 µL/min. The following gradient was used for peptide separation: from 2% B to 15% B over 3 min to 45% B over 59 min to 80% B over 3 min followed by 9 min at 80% B then back to 2% B over 1 min followed by 15 min at 2% B. Buffer A was 20 mM ammonium formate in water, pH 10 and buffer B was 20 mM ammonium formate in 90% acetonitrile, pH 10. Elution of peptides was monitored with a UV detector (205 nm, 214 nm) and a total of 36 fractions were collected, pooled into 12-24 fractions using a post-concatenation strategy and dried under vacuum.

Dried peptides were resuspended in 0.1% aqueous formic acid and subjected to LC–MS/MS analysis using an Orbitrap Eclipse Tribrid Mass Spectrometer fitted with Vanquish Neo system and a FAIMS Pro interface (all Thermo Fisher Scientific) and a custom-made column heater set to 60 °C. Peptides were resolved using a RP-HPLC column (75 µm × 30 cm) packed in-house with C18 resin (ReproSil Saphir 100 C18, 1.5 µm resin; Dr. Maisch GmbH) at a flow rate of 0.3 µL/min. The following gradient was used for peptide separation: from 2% B to 8% B over 5 min to 25% B over 70 min to 35% B over 15 min to 95% B over 1 min followed by 10 min at 95% B then back to 2% B over 1 min followed by 4 min at 2% B. Buffer A was 0.1% formic acid in water and buffer B was 80% acetonitrile, 0.1% formic acid in water.

The mass spectrometer was operated in DDA mode with a cycle time of 3 s between master scans. Throughout each acquisition, the FAIMS Pro interface switched between CVs of −40 V and −70 V with cycle times of 1.5 s and 1.5 s, respectively. MS1 spectra were acquired in the Orbitrap at a resolution of 120,000 and a scan range of 400 to 1600 m/z, AGC target set to “Standard” and maximum injection time set to “Auto”. Precursors were filtered with precursor selection range set to 400–1600 m/z, monoisotopic peak determination set to “Peptide”, charge state set to 2 to 6, a dynamic exclusion of 45 s, a precursor fit of 50% in a window of 0.7 m/z and an intensity threshold of 5e3. Precursors selected for MS2 analysis were isolated in the quadrupole with a 0.7 m/z window and collected for a maximum injection time of 35 ms with AGC target set to “Standard”. Fragmentation was performed with a CID collision energy of 30% and MS2 spectra were acquired in the IT at scan rate “Turbo”.

MS2 spectra were subjected to RTS using a human database containing 20,362 entries downloaded from UniProt on 20200417 using the following settings: enzyme was set to “Trypsin”, TMTpro16plex (K and N-term) and Carbamidomethyl (C) were set as fixed modification, Oxidation (M) was set as variable modifications, maximum missed cleavages were set to 1 and maximum variable modifications to 2. Maximum search time was set to 100 ms, the scoring threshold was set to 1.4 XCorr, 0.1 dCn, 10 ppm precursor tolerance, charge state 2 and “TMT SPS MS3 Mode” was enabled.

Subsequently, spectra were filtered with a precursor selection range filter of 400–1600 m/z, precursor ion exclusion set to 25 ppm low and 25 ppm high and isobaric tag loss exclusion set to “TMTpro”. MS/MS product ions of precursors identified via RTS were isolated for an MS3 scan using the quadrupole with a 2 m/z window and ions were collected for a maximum injection time of 200 ms with a normalized AGC target set to 200%. SPS was activated and the number of SPS precursors was set to 10. Isolated fragments were fragmented with normalized HCD collision energy set to 55% and MS3 spectra were acquired in the orbitrap with a resolution of 50,000 and a scan range of 100 to 500 m/z.

The acquired .raw files were analysed using the SpectroMine software (Biognosys AG, Schlieren, Switzerland). Spectra were searched against a human database consisting of 20,372 protein sequences (downloaded from UniProt on 2022/02/22). Standard Pulsar search settings for TMT 16 pro (“TMTpro_Quantification”) were used and resulting identifications and corresponding quantitative values were exported on the PSM level using the “Export Report” function. Acquired reporter ion intensities were employed for automated quantification and statistical analysis using the in-house developed SafeQuant R script (v2.3) (*37*). This analysis included adjustment of reporter ion intensities, global data normalization by equalizing the total reporter ion intensity across all channels, data imputation using the knn algorithm, summation of reporter ion intensities per protein and channel, and calculation of protein abundance ratios. To meet additional assumptions (normality and homoscedasticity) underlying the use of linear regression models and t-tests, MS-intensity signals were transformed from the linear to the log-scale. The summarized protein expression values were used for statistical testing of between condition differentially abundant proteins. Here, empirical Bayes moderated t-tests were applied, as implemented in the R/Bioconductor limma package (http://bioconductor.org). The resulting per protein and condition comparison p-values were adjusted for multiple testing using the Benjamini-Hochberg method.

Cell secretome (DIA): A BCA analysis was then performed to measure protein concentration in the samples and medium+FBS background was subtracted. For standard secretome analysis, a volume of medium corresponding to 30 µg protein was taken from all samples. The proteins were reduced by 10 mM DTT for 45 min and then alkylated with 50 mM IAA for 45 min in the dark and quenched by addition of 10 mM DTT. Proteins were precipitated using methanol/chloroform and then resuspended in 50 mM EPPS with 8 M urea. After dilution of urea to 4 M, LysC was added at 1:75 ratio to protein for 4 h and then urea was diluted to 1 M, before adding trypsin at the same quantity overnight. The samples were then acidified using trifluoracetic acid to pH 3, cleaned using C18 StageTips according to the manufacturer’s protocol, and vacuum dried.

For deep secretome (DeepSec) analysis, 300 µg protein (around 100 µL of secretome) was incubated with 1 mg/mL phosphatidylcholine for 1 h at 37 °C and then with 25 mg/mL of 200 nm polystyrene NPs (Polybead Microspheres 0.20µm) for 1 h at 37 °C under vortexing at 300 rpm. The incubated mixtures were then centrifuged at 14,000 g for 20 min to pellet the corona coated NPs. To remove the unbound proteins, the pellets were redispersed in 100 µL of cold PBS and centrifuged at 14,000 g for 20 min. The final pelleted samples were resuspended in 20 µL of PBS, and the proteins were reduced with 2 mM final concentration of DTT at 37 °C for 45 min and then alkylated using 8 mM final concentration of IAA for 45 min at RT in the dark. Subsequently, 0.1 µg of LysC (in PBS) was added for 4 h, followed by the same quantity of trypsin

overnight. The samples were then centrifuged at 16,000 g for 20 min at RT to remove the nanoparticles. The samples were acidified using trifluoracetic acid to pH 3, cleaned using StageTips (Thermo), and vacuum dried.

Dried peptides were resuspended in 0.1% aqueous formic acid, 0.02% DDM (n-Dodecyl-B-D-maltoside) and subjected to LC–MS/MS analysis using a timsTOF Ultra Mass Spectrometer (Bruker) equipped with a CaptiveSpray nano-electrospray ion source (Bruker) and fitted with a Vanquish Neo (Thermo Fisher Scientific). Peptides were resolved using a RP-HPLC column (100 µm × 30 cm) packed in-house with C18 resin (ReproSil Saphir 100 C18, 1.5 µm resin; Dr. Maisch GmbH) at a flow rate of 0.4 µL/min and column heater set to 60 °C. The following gradient was used for peptide separation: from 2% B to 25% B over 25 min to 35% B over 5 min to 95% B over 1 min followed by 5 min at 95% B to 2% B over 1 min followed by 3 min at 2% B. Buffer A was 0.1% formic acid in water and buffer B was 80% acetonitrile, 0.1% formic acid in water.

The mass spectrometer was operated in dia-PASEF mode with a cycle time estimate of 0.96 s. MS1 and MS2 scans were acquired over a mass range from 100 to 1700 m/z. A method with 8 dia-PASEF scans separated into 3 ion mobility windows per scan covering a 400-1000 m/z range with 25 Da windows and an ion mobility range from 0.64 to 1.37 Vs cm^2 was used. Accumulation and ramp time were set to 100 ms, capillary voltage was set to 1600 V, dry gas was set to 3 L/min and dry temperature was set to 200 °C. The collision energy was ramped linearly as a function of ion mobility from 59 eV at 1/K0 = 1.6 V s cm^{-2} to 20 eV at 1/K0 = 0.6 V s cm^{-2}.

The acquired files were searched using the Spectronaut (Biognosys v19.0) directDIA workflow against a Homo sapiens database (consisting of 20,360 protein sequences downloaded from UniProt on 2022/02/22) and 392 commonly observed contaminants. Quantitative fragment ion data (F.Area) was exported from Spectronaut. For host–pathogen secretome analyses, DIA files were searched against concatenated species-specific databases containing the human UniProt proteome together with either *F. nucleatum* or EAEC strain 042 protein sequences (O44H18strain042EAEC_UP000001407 downloaded on 2026/03/25), plus common contaminants. Proteins were assigned to host or bacterial origin based on database source annotations. Peptides mapping ambiguously across species were excluded from species-specific interpretation. Human and bacterial protein groups were subsequently separated and analyzed independently.

Proteome and secretome data processing and quality control

Cell proteome and secretome datasets were processed using a shared preprocessing workflow with dataset-specific filtering thresholds. In both datasets, after removal of contaminant proteins, proteins supported by at least two peptides and detected in more than 50% of samples within at least one condition were retained. Intensities were log2-transformed and median-centered across samples.

For the cell proteome, artificial floor-intensity values were treated as missing before transformation and normalized in each TMT channel. For the secretome, non-positive intensity values were treated as missing. Missing values were then imputed using a two-step hybrid approach consisting of k-nearest neighbor (kNN) imputation (k=3), followed by random sampling from a left-shifted Gaussian distribution parameterized from the global data distribution (downshift = 1.8 SD, width = 0.3 SD). Data quality and potential outliers were assessed using PCA, sample-wise correlation analysis, and

intensity distribution summaries. Data processing and quality assessment were performed via python [version 3.11.4] using pandas [version 2.3.3], NumPy [version 2.3.5], SciPy [version 1.17.1], scikit-learn [version 1.8.0], statannotations [version 0.7.2] and statsmodels [version 0.14.6].

Protein annotation and secretory feature analysis

Protein annotation and secretory features were assessed using UniProt annotations together with sequence-based prediction tools. Protein accessions were mapped to UniProt to retrieve protein descriptions, gene names, subcellular localization, Gene Ontology cellular-component terms, and relevant keywords. Full length protein sequences were analyzed with SignalP [version 6.0] to predict N-terminal signal peptides and with DeepTMHMM [version 1.0.57] to predict transmembrane topology. Proteins were classified as candidate secreted or extracellular proteins based on UniProt extracellular/secreted annotations or the presence of a predicted signal peptide, while proteins containing predicted transmembrane regions were annotated as membrane associated.

Differential abundance, pathway enrichment and statistical analysis

Differential abundance testing was performed in R [version 4.3.3] using limma package [version 3.58.1]. Normalized log2-transformed protein abundance matrices were modeled according to experimental condition, and predefined pairwise comparisons were tested. P values were adjusted for multiple testing using the Benjamini-Hochberg method. Proteins were considered differentially abundant according to adjusted P value (< 0.05) and arbitrary $\log_2$ fold change thresholds (> 0.5 in all analyses and >0.3 for the experiment on endolysosomal trafficking experiment).

Functional enrichment analysis was performed in Python using g:Profiler (*Homo sapiens*) via the gprofiler-official [version 1.0.0] with Gene Ontology and KEGG pathway annotations. Terms with adjusted P value < 0.05 were retained. Fold enrichment was calculated from observed versus expected overlap proportions.

For the adipocyte secretome analysis, data processing and quality control were performed using the same workflow as described for the other datasets. Proteome-wide differential abundance was assessed using Welch's two-sample t-test, followed by Benjamini-Hochberg correction for multiple testing. Because SAA1 was a predefined protein of biological interest, it was additionally assessed using a targeted exact two-sided label-permutation test. Group labels were permuted across all balanced 4-versus-4 assignments, and the absolute $\log_2$ fold-change between LPS-treated and control adipocytes was used as the test statistic. The exact permutation P value was calculated for the observed SAA1 effect. This targeted SAA1 analysis was reported separately from the proteome-wide FDR-corrected analysis.

Steatosis and fibrosis scores were calculated as defined in the corresponding figure legend. For each signature protein, $\log_2$ transformed abundance values were standardized relative to the lean group by subtracting the lean-group mean and dividing by the lean group standard deviation. The standardized values were then combined across the proteins in each signature to obtain a lean-centered steatosis or fibrosis score for each sample. Scores were compared between the MASH group and lean, resmetirom, lanifibranor, and retatrutide groups using two-sided Welch's t-test.

Protein trend analysis

To assess dose-dependent responses, protein intensities were first log_2-transformed and then z-scored across the four treatment groups (Control, LPS-C1, LPS-C2, LPS-C3). For each protein, differences between consecutive doses were examined. Proteins were classified as monotonically increased if all consecutive differences exceeded a tolerance of 0.2 SD and the overall net increase across the dose series was ≥1 SD. Monotonically decreased proteins were defined analogously. Proteins with a single turning point (increase then decrease or vice versa) were labeled as transient up/down, while flat trajectories (net change <0.2) were assigned to no change. All other patterns were categorized as mixed/other.

Data visualization

Data visualization was performed in Python [version 3.11.4] using matplotlib [version 3.10.9] and seaborn [version 0.13.2]. Volcano plots, heatmaps, Venn diagram plots, hexbin quadrant plots and pathway enrichment bubble plots were generated from normalized log_2 transformed protein abundance matrices and downstream differential or enrichment analysis results.

Cryo-TEM

Cryo-electron tomography was performed to capture three-dimensional structural information at near-native conditions. Single-axis cryo-electron tomograms were acquired using a Titan Krios TEM from Thermo Fisher Scientific. The instrument was operated at an accelerating voltage of 300 kV, providing high-resolution imaging capabilities. It was equipped with a Falcon 2 direct electron detector (DED) to enhance image quality and sensitivity. Data collection was controlled using FEI Batch Tomography Software to ensure precise and automated operation.

During the imaging process, tilt series were collected at a magnification of 59,000X, covering a tilt range from -60° to +60°. The tilt angles were incremented in steps of 2°, allowing for comprehensive sampling of the specimen's three-dimensional structure. The nominal pixel size at this magnification was 1.375 Å, providing detailed resolution of fine structural features. The defocus values were set within a range of -2 to -3 µm to optimize contrast and phase information.

Each total dose of electrons delivered per tomogram was approximately 80 electrons per Å² ($e^-/Å^2$), balancing the need for sufficient signal-to-noise ratio with minimizing radiation damage to the sample. This carefully controlled imaging protocol allowed for high-quality data collection suitable for subsequent three-dimensional reconstruction and structural analysis.

Enzyme Linked Immunosorbent Assay (ELISA)

Concentrations of IL-1β, CXCL8 and CXCL10 were measured using commercially available ELISA kits (Invitrogen, IL-1β: #BMS224-2; CXCL8: #88-8086-88; CXCL10: #KAC2361) according to the manufacturer’s instructions.

Pro-collagen Iα1 levels were measured in supernatants collected from the same PHH:SC spheroid cultures used for neutral lipid quantification (see above), using the Human Pro-Collagen I alpha 1 DuoSet ELISA (R&D Systems, #DY6220-05) following the manufacturer's protocol. Absorbance was measured at 450 and 540 nm on a SpectraMax iD3s plate reader (Molecular Devices).

Incucyte® Live-Cell Analysis

For real-time live-cell imaging, 1.25x10^5 THP1 cells seeded in 48-well plates were incubated with 1:50,000 Incucyte Cytotox (S7020, Invitrogen) for 3 h prior to treatment. Cell viability was measured every hour for 24 h using an Incucyte S3 System (Sartorius). Quantification and data generation were performed using the Incucyte 2022B software (Sartorius). Data were normalized relative to vehicle control.

Immunofluorescence microscopy

Cells were either fixed with 4% paraformaldehyde and permeabilized with 0.5% Triton X-100, or fixed with ice-cold methanol (LC3 co-straining experiments).Fixed cells were blocked 45 min in 3% BSA prior to immunostaining using the following antibodies: Calnexin (MA5-15389, Invitrogen); CXCL8 (#94407, Cell Signaling); GM130 (#12480, Cell Signaling); LC3B (#83506, Cell Signaling); MMP1 (#54376, Cell Signaling); SEC31A (#13466, Cell Signaling); Alexa Fluor 488 or 568 conjugated secondary antibodies (Thermo Fisher Scientific). Hoechst (1:2000) was used for nuclear counterstaining. Images were acquired with a Zeiss LSM800 Airyscan confocal microscope and processed using ImageJ software.

Western blot

Cell lysates were prepared in ice cold RIPA buffer (Thermo Fisher Scientific) supplemented with protease inhibitors (cOmplete; Roche), phosphatase inhibitors (PhosSTOP, Roche) and benzonase (Merck). Protein samples were denatured in Laemmli buffer at 95°C for 5 min, separated by SDS-PAGE and analyzed by Western blot following standard procedure. Antibodies used were the following: CXCL8 (#94407, Cell Signaling); LC3B (#3868; Cell Signaling); MMP1 (#54376, Cell Signaling); β-actin (#MAB-1501; Millipore).

Lipid accumulation and oxidative stress imaging

For confocal imaging, PHH:SC spheroids (6:1 ratio; 600 cells), were seeded in 384-well ultra-low attachment (ULA) plates (BIOFLOAT™, #F224384, faCellitate GmbH, Mannheim, Germany) and cultured as described above. After 7 days of FFA and test compound treatment, spheroids were incubated with CellROX™ Deep Red reagent (#C10422, Invitrogen, 5 µM final) for 30 min at 37°C. H_2O_2 (250 µM) served as a positive control for oxidative stress. Spheroids were subsequently washed with HBSS (1×), fixed in 4% (v/v) methanol-free formaldehyde for 45 min at room temperature, washed with HBSS (3X), and stained overnight with Hoechst33342 (#H3570, Invitrogen; 1:500) and BODIPY (#HY-D1614, MedChemExpress; 1 µM final). Prior to imaging, spheroids were washed again with HBSS (3X) to reduce background fluorescence. Imaging was performed on a high-content confocal microscope (Opera Phenix, Revvity) using a 20X air objective across 16 z-planes per well. Spheroid area, roundness, and mean fluorescence intensities (BODIPY: Ex 488 nm; CellROX: Ex 647 nm) were extracted using the PhenoLOGIC algorithm in Harmony software, with combined green and deep red channel fluorescence used for spheroid segmentation.

Neutral lipid quantification

For fluorometric lipid quantification, PHH:SC spheroids (6:1 ratio; 1,800 cells total) were seeded in 96-well ultra-low attachment plates (#7007, Corning). After 7 days of treatment, spheroids in 20 µL of residual culture medium were dissociated in 2.5% trypsin (Gibco, Thermo Fisher Scientific) at 37°C. Medium-only control wells were prepared identically. AdipoRed reagent (#PT-7009, Lonza) was added according to the manufacturer's instructions and incubated for 10 min at room temperature.

Fluorescence (Ex 485 nm / Em 572 nm) was measured on a SpectraMax iD3s plate reader (Molecular Devices, San Jose, CA, USA), and medium control values were subtracted from spheroid measurements to obtain corrected cellular lipid content.

Data availability

The authors declare that all data supporting the findings of this study are available within the paper and its supplementary information and data files. Proteomic data have been deposited to the ProteomeXchange Consortium (https://www.proteomexchange.org/) via the MassIVE (*38*) partner repository (https://massive.ucsd.edu/) with MassIVE data set identifier MSV000098870 and MSV000102213 and ProteomeXchange identifier PXD079920. The source data for all figures is Supplementary Data 1-16 and all datapoints are shown in the figures.

Acknowledgements

We thank XProteome Inc. for providing the small molecule reagent for the analysis of the secretome samples. We thank Dr. Eric Cascales for sharing the EAEC strains. A.A.S. was supported by a grant from the Swedish Research Council [2023-02692] and the Novo Nordisk Foundation [NNF25OC0100921]. S.P. was supported by the Swedish Cancer Society [22-2423-Pj] and the Swiss Bridge Foundation. V.M.L. acknowledges support from the ERC Consolidator Grant 3DMASH [101170408], the European Union's Horizon Europe program NEMESIS [101137405], the SciLifeLab and Wallenberg National Program for Data-Driven Life Science [WASPDDLS22:006], Cancerfonden [24-3735Pj] and the Robert Bosch Foundation, Stuttgart, Germany.

Competing Interests: M.M. discloses that (1) he is a co-founder and director of the Academic Parity Movement (www.paritymovement.org), a non-profit organization dedicated to addressing academic discrimination, violence and incivility; (2) he is a co-founder of and shareholder in Targets' Tip, AlbuDerm, and XProteome Inc.; and (3) he receives royalties/honoraria for his published books, plenary lectures and licensed patents. A.A.S. and B.B. are co-founders of XProteome, Inc. V.M.L. is co-founder, CEO and shareholder of HepaPredict AB, as well as co-founder and shareholder of Shanghai Hepo Biotechnology Ltd.

Author contributions

Conceptualization, A.A.S., S.P., M.M. and B.B.; project organization, training, resources, and funding acquisition, A.A.S., S.P., V.M.L., M.M., M.A., N.M., B.B., and M.R.; Experiments, K.F., A.W., S.W., M.A., A.K., J.J.; proteomics, D.R., A.S. and A.A.S.; cryo-TEM, H.V.; data analysis and visualization, mainly X.W., plus K.F., A.A.S., H.G., M.J., S.M.M., and S.P.; writing—original draft, X.W., S.P., M.M., V.M.L., M.A., and A.A.S.; writing—review and editing, all co-authors.

References

1. S. C. Reghupaty, N. R. Dall, K. J. Svensson, Hallmarks of the metabolic secretome. *Trends Endocrinol. Metab.* **35**, 49–61 (2024).

2. W. Wu, J. Krijgsveld, Secretome analysis: reading cellular sign language to understand intercellular communication. *Mol. Cell. Proteomics* **23**, 100692 (2024).

3. M. Stastna, J. E. Van Eyk, Secreted proteins as a fundamental source for biomarker discovery. *Proteomics* **12**, 722–735 (2012).

4. D. Hanahan, R. A. Weinberg, Hallmarks of cancer: the next generation. *cell* **144**, 646–674 (2011).

5. K. E. De Visser, J. A. Joyce, The evolving tumor microenvironment: From cancer initiation to metastatic outgrowth. *Cancer Cell* **41**, 374–403 (2023).

6. A. Rivera, M. C. Siracusa, G. S. Yap, W. C. Gause, Innate cell communication kick-starts pathogen-specific immunity. *Nat. Immunol.* **17**, 356–363 (2016).

7. R. Medzhitov, C. Janeway Jr, Innate immunity. *N. Engl. J. Med.* **343**, 338–344 (2000).

8. S. Knecht, H. C. Eberl, N. Kreisz, U. J. Ugwu, T. Starikova, B. Kuster, S. Wilhelm, An introduction to analytical challenges, approaches, and applications in mass spectrometry–based secretomics. *Mol. Cell. Proteomics* **22**, 100636 (2023).

9. C. Almeida-Marques, F. Rolfs, S. R. Piersma, I. V. Bijnsdorp, T. V. Pham, J. C. Knol, C. R. Jimenez, Secretome processing for proteomics: A methods comparison. *Proteomics* **24**, 2300262 (2024).

10. M. Dagher, G. Ongo, N. Robichaud, J. Kong, W. Rho, I. Teahulos, A. Tavakoli, S. Bovaird, S. Merjaneh, A. Tan, nELISA: a high-throughput, high-plex platform enables quantitative profiling of the inflammatory secretome. *Nat. Methods*, 1–11 (2025).

11. M. Mahmoudi, M. P. Landry, A. Moore, R. Coreas, The protein corona from nanomedicine to environmental science. *Nat. Rev. Mater.* **8**, 422–438 (2023).

12. J. E. Blume, W. C. Manning, G. Troiano, D. Hornburg, M. Figa, L. Hesterberg, T. L. Platt, X. Zhao, R. A. Cuaresma, P. A. Everley, Rapid, deep and precise profiling of the plasma proteome with multi-nanoparticle protein corona. *Nat. Commun.* **11**, 3662 (2020).

13. B. Olinger, R. Banarjee, A. Dey, D. Tsitsipatis, T. Tanaka, A. Ram, T. Nyunt, G. N. Daya, Z. Peng, M. Shrivastava, The secretome of senescent monocytes predicts age-related clinical outcomes in humans. *Nat. Aging*, 1–14 (2025).

14. A. A. Ashkarran, H. Gharibi, S. A. Sadeghi, S. M. Modaresi, Q. Wang, T.-J. Lin, G. Yerima, A. Tamadon, M. Sayadi, M. Jafari, Small molecule modulation of protein corona for deep plasma proteome profiling. *Nat. Commun.* **15**, 9638 (2024).

15. A. A. Saei, B. Ghaffari, B. Bonakdarpour, L. Sun, Y. Ge, D. R. Nisbet, V. Serpooshan, K. Kostarelos, B. Borhan, C. J. Murphy, Leveraging nanoparticle protein corona to advance plasma proteome profiling. *Nat. Commun.* **17**, 5291 (2026).

16. M. Mahmoudi, B. Ghaffari, L. Han, A. Alpaydin, N. Wills, S. Grumelot, A. Tamadon, G. Yerima, D. Ritz, A. Schmidt, Ligand-mediated proteome remodeling shapes nanoparticle protein corona composition for deep plasma profiling. BioRxiv (2026).

17. J. Jalkanen, J. Zhong, P. A. N. Nankam, N. Bhalla, M. Elmastas, J. Luo, S. Weinbrenner, S. Frendo-Cumbo, B. Pesti, W. Gourash, Cytoarchitectural multi-depot profiling reveals immune-metabolic crosstalk in human colon-associated adipose tissue. *Cell Metab.* (2026).

18. S. Sheibani, K. Basu, A. Farnudi, A. Ashkarran, M. Ichikawa, J. F. Presley, K. H. Bui, M. R. Ejtehadi, H. Vali, M. Mahmoudi, Nanoscale characterization of the biomolecular

corona by cryo-electron microscopy, cryo-electron tomography, and image simulation. *Nat. Commun.* **12**, 573 (2021).

19. S. A. Sadeghi, K. Li, Y. Yue, R. Tabatabaeian Nimavard, S. Grumelot, A. A. Saei, H. Vali, F. Fang, X. Liu, M. Mahmoudi, Integrated top-down and bottom-up proteomics enables precise characterization of proteoforms within the protein corona. *Nat. Commun.* (2026).

20. F. Teufel, J. J. Almagro Armenteros, A. R. Johansen, M. H. Gíslason, S. I. Pihl, K. D. Tsirigos, O. Winther, S. Brunak, G. von Heijne, H. Nielsen, SignalP 6.0 predicts all five types of signal peptides using protein language models. *Nat. Biotechnol.* **40**, 1023–1025 (2022).

21. S. Martinelli, E. A. Anderzhanova, T. Bajaj, S. Wiechmann, F. Dethloff, K. Weckmann, D. E. Heinz, T. Ebert, J. Hartmann, T. M. Geiger, Stress-primed secretory autophagy promotes extracellular BDNF maturation by enhancing MMP9 secretion. *Nat. Commun.* **12**, 4643 (2021).

22. S.-H. Guo, H.-F. Wang, Z.-G. Nian, Y.-D. Wang, Q.-Y. Zeng, G. Zhang, Immunization with alkyl hydroperoxide reductase subunit C reduces Fusobacterium nucleatum load in the intestinal tract. *Sci. Rep.* **7**, 10566 (2017).

23. X. Zheng, T. Gong, W. Luo, B. Hu, J. Gao, Y. Li, R. Liu, N. Xie, W. Yang, X. Xu, Fusobacterium nucleatum extracellular vesicles are enriched in colorectal cancer and facilitate bacterial adhesion. *Sci. Adv.* **10**, eado0016 (2024).

24. L. Turnbull, M. Toyofuku, A. L. Hynen, M. Kurosawa, G. Pessi, N. K. Petty, S. R. Osvath, G. Cárcamo-Oyarce, E. S. Gloag, R. Shimoni, Explosive cell lysis as a mechanism for the biogenesis of bacterial membrane vesicles and biofilms. *Nat. Commun.* **7**, 11220 (2016).

25. R. Juodeikis, S. R. Carding, Outer membrane vesicles: biogenesis, functions, and issues. *Microbiol. Mol. Biol. Rev.* **86**, e00032-22 (2022).

26. H. Zhu, M. Li, D. Bi, H. Yang, Y. Gao, F. Song, J. Zheng, R. Xie, Y. Zhang, H. Liu, Fusobacterium nucleatum promotes tumor progression in KRAS p. G12D-mutant colorectal cancer by binding to DHX15. *Nat. Commun.* **15**, 1688 (2024).

27. C. E. Gatza, A. Holtzhausen, K. C. Kirkbride, A. Morton, M. L. Gatza, M. B. Datto, G. C. Blobe, Type III TGF-β receptor enhances colon cancer cell migration and anchorage-independent growth. *Neoplasia* **13**, 758-IN28 (2011).

28. B. Zhai, Y. Zhao, Y. Fan, X. Xia, Y. Yang, Machine learning-based construction of an oxidative stress-related model reveals molecular subtypes and tumor microenvironment infiltration signatures in colon cancer. *Discov. Oncol.* **17**, 136 (2026).

29. M. W. Saif, D. Alexander, C. M. Wicox, Serum alkaline phosphatase level as a prognostic tool in colorectal cancer: a study of 105 patients. *J. Appl. Res.* **5**, 88 (2005).

30. Y. Cherrak, N. Flaugnatti, E. Durand, L. Journet, E. Cascales, Structure and activity of the type VI secretion system. *Microbiol. Spectr.* **7**, 10–1128 (2019).

31. L. Liu, S. Hao, R. Lan, G. Wang, D. Xiao, H. Sun, J. Xu, The type VI secretion system modulates flagellar gene expression and secretion in Citrobacter freundii and contributes to adhesion and cytotoxicity to host cells. *Infect. Immun.* **83**, 2596–2604 (2015).

32. S. Youhanna, A. M. Kemas, S. C. Wright, Y. Zhong, B. Klumpp, K. Klein, A. Motso, M. Michel, N. Ziegler, M. Shang, Chemogenomic screening in a patient-derived 3D fatty liver disease model reveals the CHRM1-TRPM8 axis as a novel module for targeted intervention. *Adv. Sci.* **12**, 2407572 (2025).

33. Q. Zhao, W. De Nardo, R. Wang, Y. Zhong, U. Keles, G. Sakalauskaite, L. N. Zhao, H. Tay, S. Youhanna, M. Yan, Global molecular landscape of early MASLD progression in human obesity. *Elife* **14**, RP109534 (2026).

34. C. Sommerauer, C. J. Gallardo-Dodd, C. Savva, L. Hases, M. Birgersson, R. Indukuri, J. X. Shen, P. Carravilla, K. Geng, J. N. Søndergaard, Estrogen receptor activation remodels TEAD1 gene expression to alleviate hepatic steatosis. *Mol. Syst. Biol.* **20**, 374 (2024).

35. C. C. Wu, K. A. Tsantilas, J. Park, D. Plubell, J. A. Sanders, P. Naicker, I. Govender, S. Buthelezi, S. Stoychev, J. Jordaan, Enrichment of extracellular vesicles using Mag-Net for the analysis of the plasma proteome. *Nat. Commun.* **16**, 5447 (2025).

36. A. A. Saei, A. Lundin, H. Lyu, H. Gharibi, H. Luo, J. Teppo, X. Zhang, M. Gaetani, Á. Végvári, R. Holmdahl, Multifaceted proteome analysis at solubility, redox, and expression dimensions for target identification. *Adv. Sci.* **11**, 2401502 (2024).

37. E. Ahrné, T. Glatter, C. Viganò, C. von Schubert, E. A. Nigg, A. Schmidt, Evaluation and improvement of quantification accuracy in isobaric mass tag-based protein quantification experiments. *J. Proteome Res.* **15**, 2537–2547 (2016).

38. M. Choi, J. Carver, C. Chiva, M. Tzouros, T. Huang, T.-H. Tsai, B. Pullman, O. M. Bernhardt, R. Hüttenhain, G. C. Teo, MassIVE. quant: a community resource of quantitative mass spectrometry–based proteomics datasets. *Nat. Methods* **17**, 981–984 (2020).

Supplementary Files

This is a list of supplementary files associated with this preprint. Click to download.

- SupplementaryData14.xlsx
- SupplementaryData6.xlsx
- SupplementaryData16.xlsx
- SecretomeManuscriptSuppInformation.pdf
- SupplementaryData13.xlsx
- SupplementaryData1012.xlsx
- SupplementaryData15.xlsx
- SupplementaryData15.xlsx
- SupplementaryData79.xlsx